

Temperature regime and water/hydroxyl behavior in the crater Boguslawsky on the Moon



Christian Wöhler^{a,*}, Arne Grumpe^a, Alexey A. Berezhnoy^b, Ekaterina A. Feoktistova^b, Nadezhda A. Evdokimova^c, Karan Kapoor^a, Vladislav V. Shevchenko^b

^a Dortmund Technical University, Image Analysis Group, Otto-Hahn-Str. 4, 44227 Dortmund, Germany

^b Sternberg Astronomical Institute, Universitetskij pr. 13, Moscow State University, 119234 Moscow, Russia

^c Space Research Institute, Profsoyuznaya Str. 84/32, 117997 Moscow, Russia

ARTICLE INFO

Article history:

Received 6 July 2016

Revised 9 November 2016

Accepted 20 December 2016

Available online 27 December 2016

Keywords:

Moon

Boguslawsky crater

Hydroxyl

Temperature regime

Volatiles

Infrared spectroscopy

ABSTRACT

In this work we examine the lunar crater Boguslawsky as a typical region of the illuminated southern lunar highlands with regard to its temperature regime and the behavior of the depth of the water/hydroxyl-related spectral absorption band near $3\text{ }\mu\text{m}$ wavelength. For estimating the surface temperature, we compare two different methods, the first of which is based on raytracing and the simulation of heat diffusion in the upper regolith layer, while the second relies on the thermal equilibrium assumption and uses Moon Mineralogy Mapper (M^3) spectral reflectance data for estimating the wavelength-dependent thermal emissivity. A method for taking into account the surface roughness in the estimation of the surface temperature is proposed. Both methods yield consistent results that coincide within a few K. By constructing a map of the maximal surface temperatures and comparing with the volatility temperatures of Hg, S, Na, Mg, and Ca, we determine regions in which these volatile species might form stable deposits. Based on M^3 data of the crater Boguslawsky acquired at different times of the lunar day, it is found that the average OH absorption depth is higher in the morning than at midday. In the morning a dependence of the OH absorption depth on the local surface temperature is observed, which is no more apparent at midday. This suggests that water/OH accumulates on the surface during the lunar night and largely disappears during the first half of the lunar day. We furthermore model the time dependence of the OH fraction remaining on the surface after having been exposed to the temporally integrated solar flux. In the morning, the OH absorption depth is not correlated with the remaining fraction of OH-containing species, indicating that the removal of water and/or OH-bearing species is mainly due to thermal evaporation after sunrise. In contrast, at midday the OH absorption depth increases with increasing remaining fraction of OH-containing species, suggesting photolysis by solar photons as the main mechanism for removal of the remaining OH-containing species later in the lunar day.

© 2016 Elsevier Inc. All rights reserved.

1. Introduction

The distribution and behavior of $\text{H}_2\text{O}/\text{OH}$ -containing species on the Moon has been studied by numerous researchers. At present it is considered that $\text{H}_2\text{O}/\text{OH}$ -containing compounds on the Moon may exist in several forms such as adsorbed H_2O molecules, $\text{H}_2\text{O}/\text{OH}$ -bearing minerals, and water ice. Most probable reservoirs are the regolith (preferentially its top layer), the cold traps, melt inclusions and admixtures in minerals and glasses.

The possibility that the permanently shadowed parts of the lunar polar regions might contain water ice was considered by Watson et al. (1961) and Arnold (1979). Clementine radar measure-

ments have provided the first evidence that the polar regolith in permanently shadowed cold traps may contain water ice (Nozette et al., 1996; Simpson and Tyler, 1999). The observed decrease of the epithermal neutron flux towards the poles, detected by Lunar Prospector, may be explained by the presence of hydrogen in the form of water ice in the cold traps (Feldman et al., 1998). Diviner surface temperature measurements and LAMP ultraviolet albedo spectra are consistent with the presence of exposed water frost near the lunar south pole (Hayne et al., 2015). The LCROSS impact experiment detected water vapor as well as other volatiles (light hydrocarbons, sulfur-bearing species, carbon dioxide, atoms of metals Na, Hg, Mg, and Ca) in the impact plume originating from the surface material of permanently shadowed region in the south polar crater Cabeus (Colaprete et al., 2010; Gladstone et al., 2010; Killen et al., 2010).

* Corresponding author.

E-mail address: christian.woehler@tu-dortmund.de (C. Wöhler).

The LEND instrument onboard the LCROSS spacecraft measured the hydrogen distribution in the top layer of the lunar regolith with higher spatial resolution (Mitrofanov et al., 2010a). Regions with detected high hydrogen content on the Moon do not necessarily coincide with permanently shadowed regions (Mitrofanov et al., 2010b, 2012). The reasons of absence of such coincidence are not clear yet. Pumping may be responsible for presence of water ice subsurface deposits not only in permanently shadowed regions, but also in illuminated lunar polar regions (Schorghofer and Aharonson, 2014).

The epithermal neutron flux is lower at the pole-facing slopes of illuminated polar lunar craters (Mitrofanov et al., 2010b). Such suppression of the neutron flux can be explained by an increased content of hydrogen-containing volatile species in the upper regolith layer of about 1 m thickness. Suppression of the neutron flux in surface parts inclined towards the poles suggests that the low solar irradiation and the resulting low temperature in these regions leads to an increased stability of volatile species (McClanahan et al., 2015).

For deeper understanding of behavior of volatile species on the Moon sources and sinks of these species must be studied. The major sources of the lunar volatiles are the solar wind (Crider and Vondrak, 2000; Starukhina and Shkuratov, 2000; Starukhina, 2006), impacts of comets and asteroids (Shevchenko, 1996, 1999; Berezhnoi and Klumov, 1998; Berezhnoy et al., 2003; Ong et al., 2010; Prem et al., 2015), and degassing of the lunar interiors (Boyce et al., 2010; Saal et al., 2008; Hauri et al., 2015). Solar wind sputtering is considered as an important mechanism of delivery of volatiles, including OH, to the lunar exosphere (Wurz et al., 2007). Upper limit of the OH content in the lunar exosphere, about 10^4 cm^{-3} , is in agreement with predictions of sputtering model (Wang et al., 2015). Main mechanisms of removal of surface volatiles to the lunar exosphere are thermal desorption (Poston et al., 2015) and photolysis (Mitchell et al., 2013). Volatile species can migrate from illuminated polar regions to cold traps via ballistic hops in the lunar exosphere (Crider and Vondrak, 2000).

Based on the analysis of M^3 /Chandrayaan-1 infrared hyperspectral data, presence of $\text{H}_2\text{O}/\text{OH}$ -containing species in the uppermost sunlit layer of the lunar regolith was established. These data reveal a 2.8–3.0 μm absorption band being typical of $\text{H}_2\text{O}/\text{OH}$ -bearing materials and show an increase of the band depth from low to high latitudes (Pieters et al., 2009). Other infrared studies confirmed these findings (Clark et al., 2009; Sunshine et al., 2009; McCord et al., 2011). For careful estimation of weak $\text{H}_2\text{O}/\text{OH}$ 2.8–3.0 μm absorption band depth careful removal of thermal component from infrared M^3 spectra is required (Pieters et al., 2009).

Thus, the illuminated lunar polar regions are interesting for studying the behavior of surface polar volatiles. In this paper we plan to consider $\text{H}_2\text{O}/\text{OH}$ behavior in illuminated lunar polar regions, based on analysis of Chandrayaan-1 Moon Mineralogy Mapper (M^3) infrared spectra and the temperature regime at the example of the crater Boguslawsky. We will study also the possibility of the existence in considered region of some volatile compounds, which are less volatile than water ice, such as metals Hg, Na, Mg, and Ca. The crater Boguslawsky has been considered as a Luna-Glob landing site candidate (Ivanov et al., 2014). The crater Boguslawsky with its diameter of about 95 km is located in the southern polar region near the southern edge of the South-Pole-Aitken basin distant rim (Ivanov et al., 2014). Detailed morphological and geological analysis of the Boguslawsky crater was performed by Ivanov et al. (2014, 2015a, 2015b). As the crater Boguslawsky is located at latitudes of 71–75° and the slope of its walls is about 10°, the crater is entirely illuminated by the Sun during the lunar day and no evident permanent shadowed regions are expected there. According to LEND/LRO data analysis, neutron counts for the crater Boguslawsky are higher than some nearby hydrogen-rich regions,

thus indicating lower abundances of hydrogen-containing species (Litvak et al., 2012). Comparison of the epithermal neutron flux distribution map for the considered region (Mitrofanov et al., 2012) with the corresponding geological map did not reveal any correlation (Ivanov et al., 2014). Thus, in the Boguslawsky crater area it will be unlikely to detect water/hydroxyl-containing subsurface deposits (Ivanov et al., 2014). However, Boguslawsky crater is suitable for studies of diurnal behavior of surface $\text{H}_2\text{O}/\text{OH}$ -containing species in illuminated lunar polar regions, because analysis of dependence of 2.8–3.0 μm absorption band depth on time can allow to determine main mechanisms of sinks of surface volatiles during the lunar day.

2. Methods for estimation of the lunar surface temperature

Depending on the local temperature of the lunar surface, the M^3 radiance spectra contain a thermal emission component of variable strength which starts to become significant at a wavelength of about 2.2 μm and is especially important in the longer-wavelength domain of 2.8–3.0 μm in which the water and hydroxyl (OH) absorption features are located (Pieters et al., 2009; Clark et al., 2011). It is thus necessary to compensate for the local surface temperature before any interpretation of the spectral reflectance is possible. The OH absorption depth inferred from M^3 reflectance spectra thus strongly depends on the method used for estimating the local surface temperature.

The method of Clark et al. (2011) consists of a rather complex iterative procedure which linearly approximates parts of the reflectance spectrum and treats differences between these approximations and the observed spectrum as being due to thermal emission. It is noted by Clark et al. (2011) that inaccurate temperature estimates may occur for spectra exhibiting strong pyroxene absorptions and that in many lunar regions the thermal emission contribution in the wavelength range of the OH absorption features is not fully compensated. Recent studies by Bandfield et al. (2016) and Li and Milliken (2016) have confirmed that the temperature estimation method by Clark et al. (2011) tends to result in an incomplete removal of the thermal emission component of the M^3 reflectance spectra.

A comparably simple method for estimating the lunar surface temperature is proposed by Wöhler et al. (2014). They model the radiance emitted by the surface at wavelengths beyond 2.4 μm as the weighted sum of a standard lunar sample radiance spectrum and a blackbody spectrum. The estimated temperatures are systematically too low for surfaces temperatures below 250–280 K. A direct comparison to the method of Clark et al. (2011) has shown similar results (Wöhler et al., 2014). Li and Milliken (2016) proposed another purely data driven approach. The radiative transfer based thermal emission model of a particulate medium by Hapke (2005) and the reflectance model by Hapke (1981) are used to derive an equation of the observed radiance that depends only on the single-scattering albedo of Hapke's model and the surface temperature. In addition to the M^3 observations, they use a power law to model the reflectance at 2.54 μm based on the reflectance at 1.55 μm . This relation is used to constrain the optimization problem and derive a surface temperature. While being more accurate than the method by Clark et al. (2011), the new method still falls short on locations rich in pyroxene, olivine or spinel and at high incidence angles.

Due to the shortcomings of the surface temperature estimation methods previously used for removing the thermal emission component from M^3 spectra, we have developed in this work two different approaches. The first method relies on a raytracing-based approach to computing the incident solar energy per surface element and on physical modeling of the flow of thermal energy within the lunar soil by solving the heat diffusion equation. The

second method is similar to the thermal equilibrium based technique proposed by Shkuratov et al. (2011), where we derive the local surface shape, spectral reflectance and emissivity properties from Moon Mineralogy Mapper (M^3) measurements using the surface recovery methods of Grumpe et al. (2014) and Grumpe and Wöhler (2014).

2.1. Raytracing and heat diffusion based model for surface temperature estimation

Investigations of the physical properties of the surface of the Moon started with space missions using ground-based measurements of its optical, thermal, and radio emission. These studies have suggested that the soil of the Moon has a porous structure and a very low thermal conductivity (Piddington and Minnet, 1949; Linsky, 1966; Lucas et al., 1967; Keihm and Langseth, 1973).

The hypothesis about a two-layer structure of the surface layer of the Moon was first proposed by Piddington and Minnet (1949) who investigated the thermal emission of the Moon at 1.25 cm wavelength. According to their data, confirmed subsequently by other measurements (Linsky, 1966; Keihm and Langseth, 1973), the surface of the Moon is cooled uniformly: the temperature falls rapidly at sunset, and then decreases slowly during the night. This phenomenon is possible in the presence of an insulating surface layer thickness of a few cm with low thermal conductivity, under which there is a layer with a higher heat conductivity. Median grain sizes for soils from returned lunar samples are found to be in the range between 50 and 800 μm (McKay et al., 1991).

For calculations of temperature regime of the crater Boguslawsky, several models of the lunar regolith, described below, were applied. The two-layer model was used by Vasavada et al. (1999) in order to calculate the temperature in craters near the poles of the Moon and Mercury. According to this model, the upper layer of the lunar regolith has a thickness of 2–3 cm and is characterized by a low density (1000–1300 kg/m^3) and a low thermal conductivity. The lower layer has an average thickness of 3–5 m, with an average density of 1800 kg/m^3 and a high thermal conductivity. The regolith thermal conductivity $k(x, T)$ is composed of the solid conductivity $k_1(x, T)$ and radiation heat transfer conductivity $k_2(x, T)$:

$$k(x, T) = k_1(x, T) + k_2(x, T), \quad (1)$$

where

$$k_2(x, T) = \chi k_1(x, T) (T/350)^3 \quad (2)$$

In this two-layer model k_1 and χ values are equal to $9.22 \times 10^{-4} \text{ W m}^{-1} \text{ K}^{-1}$ and 1.48 for upper layer and $9.3 \times 10^{-3} \text{ W m}^{-1} \text{ K}^{-1}$ and 0.073 for lower layer (Vasavada et al., 1999). The relationship between lunar regolith heat capacity $c(T)$ and regolith temperature for the temperatures that do not exceed 350 K comes from Ledlow et al. (1992):

$$\begin{aligned} C(T) = & 0.1812 + 0.1191 ((T - T_{300})/T_{300}) \\ & + 0.0176 ((T - T_{300})/T_{300})^2 + 0.2721 ((T - T_{300})/T_{300})^3 \\ & + 0.1869 ((T - T_{300})/T_{300})^4, \end{aligned} \quad (3)$$

where T_{300} is equal to 300 K.

Vasavada et al. (2012) suggested the absence of a sharp boundary between the surface layers. According to their hypothesis, the thermal properties of the soil change gradually and do not have a sharp transition at a depth of 2 cm. The regolith density $\rho(x)$ and thermal conductivity $k(x, T)$ in this model are given by

$$\rho(x) = \rho_d - (\rho_d - \rho_s) \exp(-x/0.06) \quad (4)$$

$$k(x, T) = k_d - (k_d - k_s) \exp(-x/0.06) + \chi k_s (T/350)^3, \quad (5)$$

where $\rho_s = 1300 \text{ kg/m}^3$ is the surface regolith density and $\rho_d = 1800 \text{ kg/m}^3$ is the regolith density at the deep boundary, $k_s = 0.0006 \text{ W m}^{-1} \text{ K}^{-1}$, $k_d = 0.007 \text{ W m}^{-1} \text{ K}^{-1}$, and $\chi = 2.7$.

The emissivity ε is the ratio of the thermal radiation from a surface M_e to the radiation from an ideal black surface M_e^0 at the same temperature as given by the Stefan–Boltzmann law:

$$\varepsilon = M_e/M_e^0. \quad (6)$$

Thus, ε value is an important parameter for transition from measured infrared flux from the lunar surface to surface temperature. The emissivity was estimated as 0.95 by Greenhagen and Paige (2006). Ran and Wang (2014) investigated the dependence of the lunar surface temperature on the surface emissivity. They used the variable emissivity model described by Birkebak (1972) and the constant emissivity model, where the emissivity was varied over the interval between 0.9 and 1 at an increment of 0.01, and their results show that the best agreement between simulated surface temperatures and surface temperatures derived from Diviner measurements is achieved by using different constant emissivity values during the lunar day. The optimal value of emissivity is equal to 0.97 and 0.94 during sunrise and sunset, and midday, respectively.

However, recent studies have revealed the existence of differences between the values of the surface temperatures obtained by the LRO Diviner radiometer and the temperature values calculated by solving the equation of heat transfer for the equatorial regions of the Moon (Vasavada et al., 2012; Ran and Wang, 2014). The maximum difference occurs at sunrise and sunset (then the solar incidence angle is high) and is about 50 K according to Ran and Wang (2014) or 25 K according to Vasavada et al. (2012). Notably, only Diviner channels 6–9 from 12.5 μm to beyond 100 μm are useful for determining a surface temperature (Sullivan, 2011). These brightness temperatures might be interpreted as a surface temperature when assuming an emissivity of 1. According to the analysis of Bandfield et al. (2016) there typically is a significant variation in brightness temperature of about 40 K between channels 6–9 for high incidence angles around 75° (as given around midday in the Boguslawsky region).

In the utilized models the flux of direct solar radiation on each illuminated surface element, the internal heat flux, the flux which is reflected from the nearby sunlit elements and the infrared flux from the nearby heated elements at each moment in time were taken into account based on an approach previously used by Carruba and Coradini (1999) and Vasavada et al. (1999). Reflected flux and infrared flux from nearby sunlit elements were calculated using the approach of Ueno et al. (1991). The Moon's surface is assumed as a Lambert scatterer. The surface temperature and the temperature distribution with depth in subsurface layer of regolith is determined by solving the nonlinear heat-diffusion equation similar to Vasavada et al. (1999), applying the method of finite differences. The heat balance of the regolith surface layer determined by solution of the one-dimensional time-dependent heat-diffusion equation

$$c(T)\rho(x) \frac{dT}{dt} = \frac{d}{dx} \left(k(x, T) \frac{dT}{dx} \right) \quad 0 < x < l \quad (7)$$

with the boundary conditions

$$k(x, T) \frac{dT(x, T)}{dx} \Big|_{x=0} = \varepsilon \sigma T^4(0, t) - (1 - a)F_1(t) \quad (8)$$

$$\frac{dT}{dx} \Big|_{x=l} = F_0 \quad (9)$$

and with the initial condition $T(x, 0) = T_0$, where $c(T)$ is the heat capacity, $\rho(x)$ is the density, $k(x, T)$ is the regolith thermal conductivity, a is the albedo of the surface, ε is the infrared emissivity of

the regolith, l is the typical depth of the heat penetration, σ is the Stefan–Boltzmann constant, $F_l(t)$ is the solar radiation flux, and F_0 is the lunar heat flux assumed to be 0.016 W m^{-2} in accordance with Langseth et al. (1976). The typical depth of heat penetration is given by

$$l = \sqrt{k(x, T)t/\pi\rho(x)c(T)} \quad (10)$$

where $k(x, T)$ is the regolith thermal conductivity and t the time period. To solve the heat-diffusion Eq. (1), we have taken into account the direct solar flux incident on each illuminated element of the surface, flux reflected from the other illuminated elements, flux of infrared radiation emitted from other elements and the internal thermal flux. These values depend on the solar incidence angle, the slope and orientation of the surface and the angular elevation of the visible horizon. We do not take into account the thermal flux from the adjacent elements of the surface; this flux can be ignored because of the low thermal conductivity of the lunar regolith. The initial temperature at the beginning of calculations at all studied regions was assumed to be 100 K. To reduce the influence of the initial set of the temperature distribution, the calculations were performed for 20 lunar days. Since the upper boundary condition is nonlinear in the temperature, the temperature at the surface at each time step was calculated by the method of simple iteration. Eq. (7) was solved by the finite difference method for the explicit scheme. In our calculations we used a time period equal to one lunar day. To determine the position of the Sun at each time step, its incidence angle and the azimuth angle were calculated. This allows for taking into account the input flux at the surface element and the reflected infrared radiation from all neighboring illuminated surface elements visible from the considered element at a given time.

The studied region of crater Bogulawsky was divided into a grid of surface elements, where the steps in longitude and latitude were taken as 0.15° and 0.05° , respectively. The total number of the elements of the area of the crater is 10,000. The height, slope and azimuthal orientation of each surface element were calculated based on the gridded LOLA digital elevation model (DEM) (Neumann, 2016; data download from <http://ode.rsl.wustl.edu/moon/>) using the algorithm described by Zevenbergen and Thorne (1987) (see Section 4.1).

2.2. Thermal equilibrium based method for surface temperature estimation

Another used approach is the thermal equilibrium based method for surface temperature estimation. This approach closely follows Shkuratov et al. (2011) and will be called thermal equilibrium (TE) model in the following. Assuming thermal equilibrium, the local surface temperature T_{surf} is given by

$$T_{\text{surf}} = T_0 \sqrt[4]{(1 - A_{\text{dh}}) \cos i} \quad (11)$$

where $T_0 = \sqrt[4]{C_{\text{sun}}/\sigma_B} \approx 394$ K is the temperature of a perfectly absorbing surface which is illuminated by normally incident radiance, $C_{\text{sun}}=1367 \text{ W/m}^2$ is the solar constant at a heliocentric distance of 1 AU, $\sigma_B=5.67 \cdot 10^{-8} \text{ W/m}^2 \text{ K}^4$ is the Stefan–Boltzmann coefficient and i is the angle of incidence. The directional hemispherical albedo

$$A_{\text{dh}} = \frac{1}{C_{\text{sun}}} \int_0^\infty E_0(\lambda) r_{\text{dh}}(i, \lambda) d\lambda \quad (12)$$

depends on the solar spectral irradiance $E_0(\lambda)$ and the directional-hemispherical reflectance $r_{\text{dh}}(i, \lambda)$. To model the local surface reflectance, we use the Hapke model (Hapke, 1981, 1984, 2002, 2012). Since the M³ data covers the wavelength range from 420 nm

to 3000 nm, we split the integral into three parts

$$A_{\text{dh}} = \frac{1}{C_{\text{sun}}} \left(\int_0^{420 \text{ nm}} E_0(\lambda) r_{\text{dh}}(i, \lambda) d\lambda + \int_{420 \text{ nm}}^{3000 \text{ nm}} E_0(\lambda) r_{\text{dh}}(i, \lambda) d\lambda + \int_{3000 \text{ nm}}^\infty E_0(\lambda) r_{\text{dh}}(i, \lambda) d\lambda \right). \quad (13)$$

The second integral corresponds to the wavelength range of the M³ instrument. Consequently, we estimate the reflectance properties of the Hapke model, i.e. the single-scattering albedo and possibly the single-scattering phase-function, according to the method by Grumpe et al. (2015) and the M³ data. Notably, the corrected M³ reflectance is now known. We thus use the current temperature estimate to compensate for the surface temperature and estimate the surface reflectance properties. Based on the estimated reflectance parameters, we obtain directional-hemispherical reflectance.

Since the lunar reflectance spectra show a parabolic shape, we fit a second order polynomial to the reflectance estimate and extrapolate the reflectance into the lower wavelength range. In case of the wavelength range above 3000 nm the reflectance is known to drop and thus an extrapolation is not feasible. In addition, the solar irradiance drops in the wavelength range above 3000 nm. We thus use a constant $r_{\text{dh}}(i, \lambda > 3000 \text{ nm})=0.16$ as a first order approximation.

2.3. Correction for surface roughness

The observed surface temperature highly depends on the roughness of the surface. The effect of small-scale surface roughness, i.e. the topography of unresolved surface areas, has been subject of several studies (e.g. Lagerros, 1998; Davidsson et al., 2015; Bandfield et al., 2016). In general, the radiance observed by one sensor element is composed of a superposition of the reflected irradiance and the thermal emission of the surface itself. Since the small-scale surface roughness is not resolved by the sensor element, the thermal emission component of the spectrum is composed of several thermally emitting surface patches of possibly different temperatures, i.e. the total thermal emission may be interpreted as a superposition of many single-temperature thermal emission spectra. While the emission spectrum of one temperature may be modeled by the thermal emission spectrum of a black body, the sum of several black body emission spectra does not follow Planck's law (Davidsson et al., 2015). The effect clearly depends on the surface roughness, which is commonly measured by the root mean squared (RMS) slope, and the zenith angle of the incident light rays with respect to a flat surface. If the zenith angle is close to zero, many small surface elements will be tilted away from the incident light rays and thus receive less energy. The resulting thermal emission spectrum is significantly smaller than the emission spectrum of the flat surface. For large zenith angles, in contrast, many small surface patches will be tilted towards the incident light rays and thus show an increased thermal emission. Consequently, the effect of surface roughness has to be considered before interpreting spectral absorption features in the 3 μm range.

To compensate for small-scale surface roughness, we apply a statistical approach similar to the method used by Davidsson et al. (2015). We produce Gaussian random surfaces using the method of Muinonen and Saarinen (2000) which resemble the unresolved rough surface. The method is detailed in Appendix A.

To estimate the smallest spatial scale on which lateral heat diffusion in the lunar regolith is negligible given the duration the lunar day, we solved the one-dimensional heat diffusion Eq. (7) with the physical parameters stated in Section 2.1 for a slab of regolith of length s whose left and right half has an initial temperature of 380 K and 100 K, respectively. For a value of $s=0.03 \text{ m}$ the temperature difference between the left and the right half of the slab falls

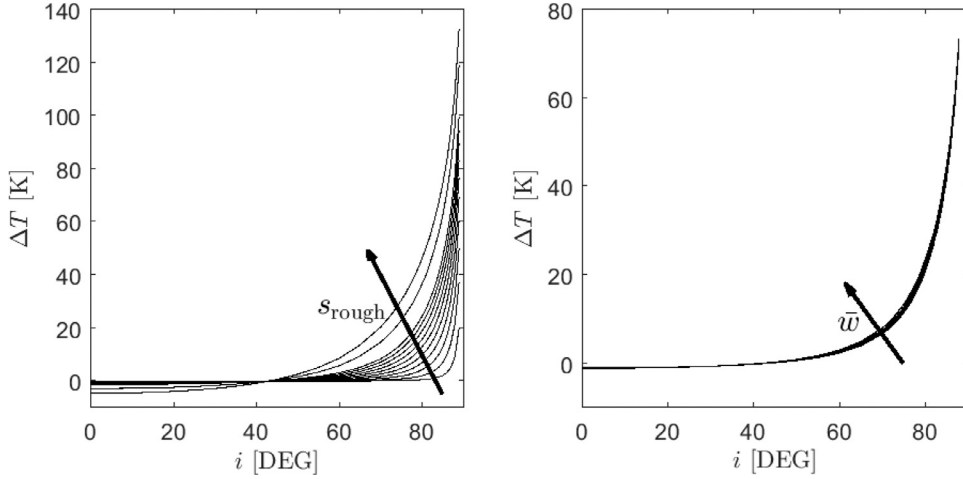


Fig. 1. Difference between the effective temperature of a single black body emission spectrum adapted to the rough surface thermal emission spectrum and the temperature of a flat surface. The temperature difference is shown for lunar sample 62,231, a typical highland reflectance spectrum, for the RMS slope values $s_{\text{rough}} \in \{1, 2, 3, 4, 5, 6, 7, 8, 9, 10, 15, 20\}$ degrees (left). An increasing roughness leads to an increasing underestimation of the thermal emission spectrum for incidence angles exceeding 40° and an increasing overestimation of the thermal emission spectrum for incidence angles below 40° . In addition, the temperature difference increases with the mean single-spectrum albedo \bar{w} , shown here for $s_{\text{rough}} = 9^\circ$ and \bar{w} values between 0.2773 and 0.7423 inferred from the 19 LSCC spectra).

below 1 K after a relaxation time τ_r of approximately 24 hours, and it follows from the structure of the heat diffusion Eq. (7) that the relaxation time τ_r is proportional to the squared slab size s^2 . The regolith surface roughness depends on the regarded spatial scale (Helfenstein and Shepard, 1999). Because the relaxation time for $s = 0.03$ m corresponds to roughly 10% of the duration of the lunar day, we will consider 0.03 m as the reference scale whose associated roughness value will be adopted for surface temperature correction.

According to Helfenstein and Shepard (1999), the RMS slope of lunar terrain on scales larger than 0.03 m is less than 9° . Consequently, we construct synthetic square surfaces of 19,600 pixels where each pixel has an edge length of 0.03 m. The parameter l_z controls the width of the Gaussians, i.e. the size of the roughness structures. The full width at half maximum of the Gaussian is approximately $2.35 l_z$ and we set $l_z = 1$ pixel. The Gaussian random surfaces do not have a preferred azimuthal direction and thus the heat distribution depends only on the zenith angle i of the sun with respect to the flat surface element, the RMS slope s_{rough} , and the surface material. In general, the zenith angle e of the sun with respect to the flat surface element is important for the directional emissivity. For hyperspectral data such as the M³ data, the sensor is close to nadir view and thus $e=0$ is a constant. We vary i in steps of 1° between 0° and 5° in steps of 5° between 5° and 70° and in steps of 1° between 70° and 89° . The RMS slope is set to be $s_{\text{rough}} \in \{1, 2, 3, 4, 5, 6, 7, 8, 9, 10, 15, 20\}$ degrees. To simulate the spectral behavior of the lunar surface, we use the bi-directional reflectance measurements of the Lunar Soil Characterization Consortium (LSCC, Taylor et al., 1999; <http://www.planetary.brown.edu/relabdocs/LSCCsoil.html>). The bi-directional reflectance spectra of the LSCC data are measured in the wavelength range 300–2600 nm. We fit a linear extrapolation to the wavelength range 2500–2600 nm and extend the spectrum up to 3000 nm. Furthermore, we fit a linear extrapolation to the standard deviation of the LSCC data in the wavelength range 2000–2600 nm and add Gaussian noise of the estimated standard deviation to the extrapolated bi-directional reflectance. The surface temperature of each facet is then obtained using the thermal equilibrium based method described in Section 2.2 and the per-square-meter thermal emission spectrum of a rough surface is computed

by summing the individual facets' emission spectra weighted by their area and normalizing the emission spectrum to the area of the random surface. The procedure is repeated for ten random surfaces for each bi-directional reflectance spectrum of the LSCC database and the average emission spectrum is determined.

The M³ wavelength range is limited to <3000 nm and one thus only observes the rising flank of the thermal emission spectrum. Although this observed emission spectrum is not a single black body emission spectrum, it shows a strong similarity across this limited wavelength range. We thus fit a black body emission spectrum with an effective temperature T_{eff} to the emission spectrum of the rough surface and determine the temperature difference between T_{eff} and the temperature of a flat surface. Fig. 1 shows that this temperature difference depends on i , s_{rough} , and the mean single-scattering albedo of the LSCC spectrum. We thus use a linear interpolation to obtain the temperature difference for each M³ measurement based on i and the mean single-scattering albedo. According to Helfenstein and Shepard (1999), the RMS slope is set to $s_{\text{rough}} = 9^\circ$.

The proposed method does not include self-heating of the surface facets, i.e. the thermal flux of one facet heating another facet. Furthermore, it implies a constant heliocentric distance of 1 AU and does not detect shadows. Therefore, we applied the temperature simulation described in Section 2.1 to one random surface ($s_{\text{rough}} = 9^\circ$) using two illumination conditions of the M³ observations of the lunar crater Boguslawsky. We then computed the single-scattering albedo of lunar sample 62231, which is a typical lunar highland spectrum. Based on this single-scattering albedo, the Hapke model predicts a reflectance, and we used the ASTM Air Mass Zero Spectrum Reference E-490-00 solar irradiance spectrum (<http://rredc.nrel.gov/solar/spectra/am0/>) to compute a synthetic radiance spectrum. The true thermal emission spectra are then added to the synthetic radiance, respectively, yielding two synthetic observations of a rough surface. The true emission spectra and the single black body fits are given in Fig. 2a-b. Fig. 2c-f show the true reflectance spectra (solid line), the reflectance estimated based on a flat surface (dashed line), and the reflectance estimated based on the proposed simple correction model (dash-dotted line). It is evident that the proposed model almost completely takes into account the effects of surface roughness.

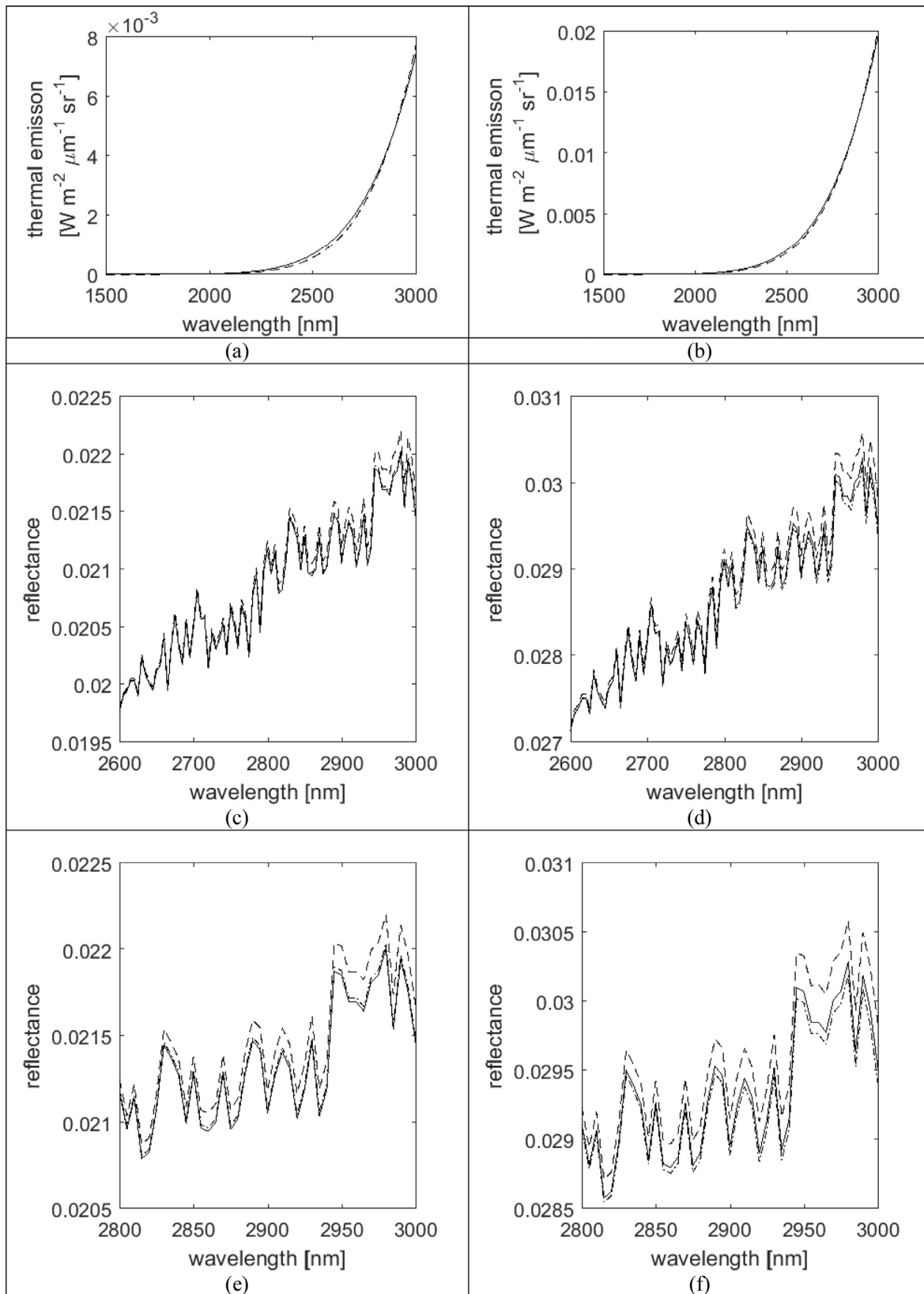


Fig. 2. Evaluation of the surface roughness model. (a)–(b) Simulated thermal emission spectrum of a rough surface (solid line) and single black body emission spectrum adapted to the thermal emission spectrum (dashed line). (c)–(d) True (solid line) and estimated reflectance spectra using a flat surface (dashed line) and the proposed simple model (dash-dotted line), respectively. (e)–(f) Close-up of the 2800–3000 nm wavelength range.

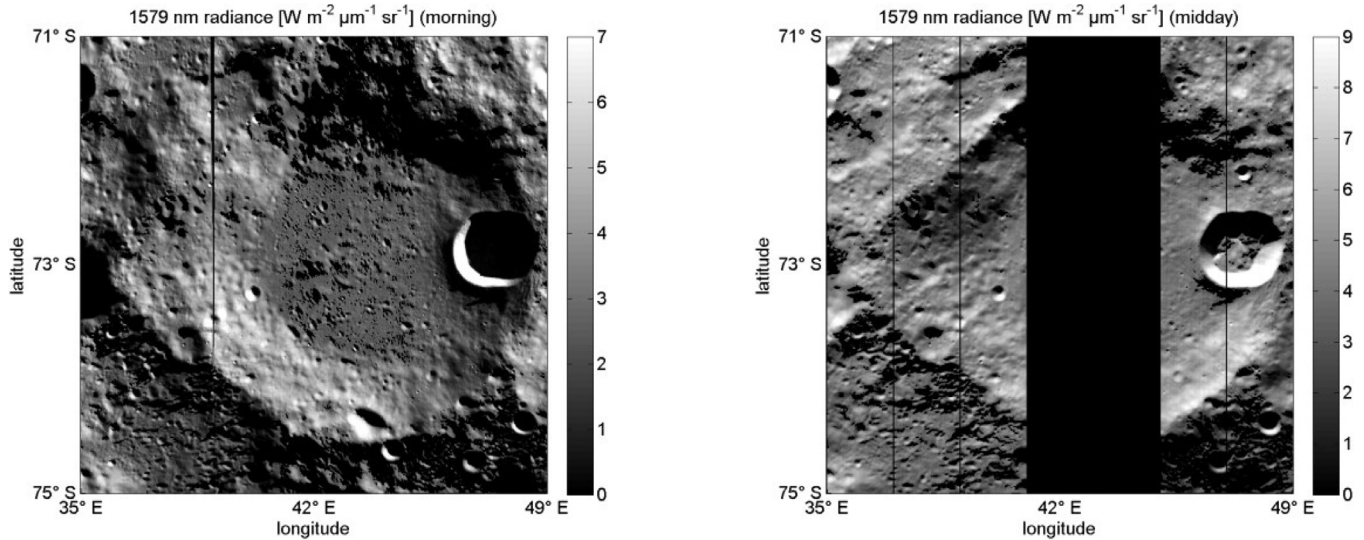


Fig. 3. M^3 radiance at 1579 nm (channel 50) in the morning (left image, local time is 8 h 24 m; average solar incidence angle is 79°) and at midday (right image, local time is 13 h 12 m; average solar incidence angle is 73°).

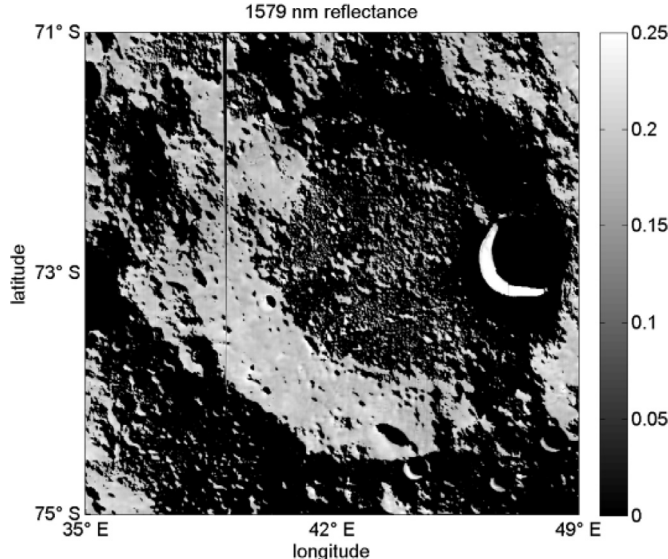


Fig. 4. Thermally and topographically corrected M^3 spectral reflectance at 1579 nm (channel 50) of the Boguslawsky region, inferred from the available morning and midday radiance data. Black denotes pixels of low M^3 radiance corresponding to shadows and slopes away from the sun, associated with a low-signal-to-noise ratio. The Boguslawsky region exhibits a nearly uniform reflectance.

3. Processing of M^3 spectral reflectance data

The first step of our routine for processing the M^3 data consists of the construction of a DEM of high resolution, which is the basis for the subsequent estimation of the surface temperature, subtraction of the thermal emission component and normalization of the spectral reflectance to a uniform illumination and viewing geometry. For more details on this procedure see Grumpe et al. (2014), Wöhler et al. (2014), Grumpe and Wöhler (2014).

3.1. DEM construction

Our DEM construction method relies on the combination of a reference DEM of a lower lateral resolution than that of the M^3 image data with a shape from shading approach which is based on

the M^3 spectral radiance data. On large spatial scales, the resulting refined DEM behaves like the reference DEM, while the shape from shading component governs its appearance on small spatial scales. This combined approach has been described in detail recently (Grumpe et al., 2014; Grumpe and Wöhler, 2014), such that we provide only a short overview here.

Given the illumination and viewing directions and a model of the direction-dependent intensity of the light reflected from the surface (the so-called reflectance function), the shape from shading technique estimates the local normal vector of the surface such that the modeled surface reflectance corresponds to the observed reflectance (Horn, 1990). The surface is inferred from the set of local normal vectors, equivalently expressed by the surface gradients, by integration. A classical and physically reasonable assumption incorporated into the corresponding optimization procedure is that the surface gradients are supposed to form an integrable vector field (Horn, 1990). In the scenario regarded here, the reflectance function introduced by Hapke (1984, 2002) is used. The desired correspondence of the refined DEM on large spatial scales with the reference DEM is expressed by Grumpe and Wöhler (2014) as an appropriate error term involving the mean squared difference between the low-pass components of the reference DEM and those of the current version of the refined DEM, which is minimized together with the mean squared difference between the modeled and the observed radiance image and an error term describing the degree of non-integrability of the surface gradients using an interactive relaxation algorithm. Together with the refined DEM, our approach also yields an estimate of the local surface albedo, expressed by the single-scattering albedo of the model by Hapke (2002). Several pixel-synchronous images can be used after application of a co-registration technique which relies on the surface gradients estimated by shape from shading individually for each image. For a detailed description of our DEM construction framework, see Grumpe et al. (2014), Grumpe and Wöhler (2014).

Here we will use as a reference DEM the GLD100 data set introduced by Scholten et al. (2012), which has a nominal lateral resolution of 100 m but for which an effective lateral resolution of about 1.5 km has been determined (Scholten et al., 2012). For shape from shading analysis, the M^3 hyperspectral images with their resolution of 140 m (Pieters et al., 2009) are used. For the central part of the Boguslawsky region, only M^3 spectral radiance images acquired at local lunar morning are available, while for its eastern and western

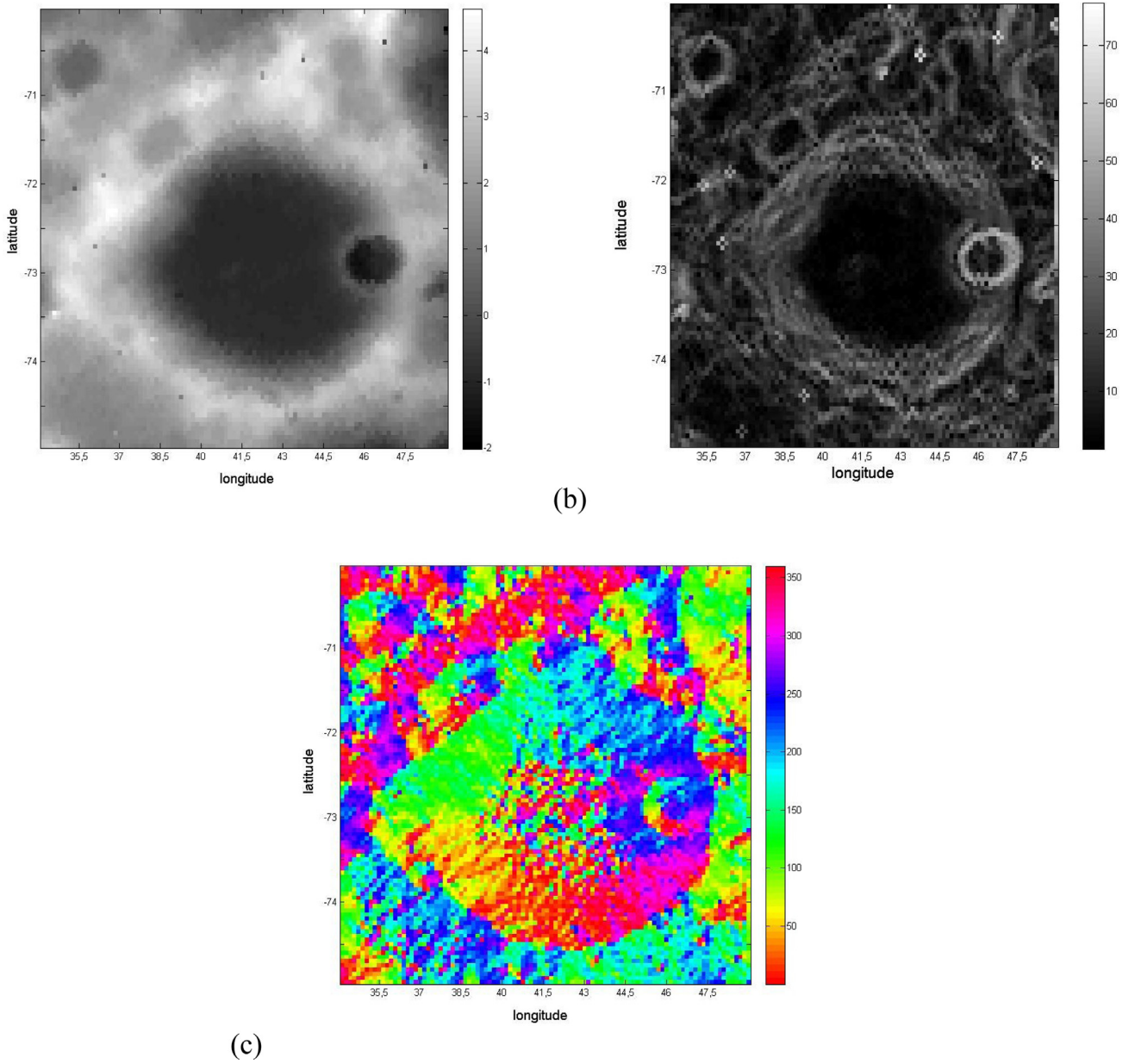


Fig. 5. (a) LOLA DEM, (b) slope, (c) azimuthal surface orientation of the Boguslawsky region.

part the M³ data set contains images taken at local lunar morning and midday (Fig. 3).

3.2. Removal of the thermal emission component

The observed spectral radiance is a superposition of the reflected solar spectral irradiance and the thermal emission spectrum of a blackbody $B(\lambda, T_{\text{surf}})$ at temperature T_{surf} . Consequently, L_{obs} amounts to

$$L_{\text{obs}}(\alpha, i, e, \lambda, T_{\text{surf}}) = E_0(\lambda)r(\alpha, i, e, \lambda) + \varepsilon_{\text{dir}}(e, \lambda)B(\lambda, T_{\text{surf}}) \quad (14)$$

where $r(\alpha, i, e, \lambda)$ is the bi-directional reflectance. It depends on the same local surface reflectance properties as the directional-hemispherical reflectance, the phase angle α , the incidence angle i , and the emission angle e . Assuming thermal equilibrium, the directional emissivity, or emittance, $\varepsilon_{\text{dir}}(e, \lambda)$ may be obtained ac-

cording to Kirchhoff's law and is given by (Nicodemus, 1965)

$$\varepsilon_{\text{dir}}(e, \lambda) = 1 - r_{\text{hd}}(e, \lambda). \quad (15)$$

The hemispherical-directional reflectance $r_{\text{hd}}(e, \lambda)$ is modeled using the Hapke model. The directional-hemispherical reflectance has the same functional dependence on i that the hemispherical-directional reflectance has on e (Hapke, 2012). Consequently, $r_{\text{hd}}(e, \lambda)$ is evaluated the same way as $r_{\text{dh}}(i, \lambda)$ by interchanging the angles.

Eqs. (11)–(15) highly depend on the spectral reflectance of the local surface. The measured radiance, however, includes the thermal emission component. Therefore, we suggest an iterative approach. Initially, we estimate the local surface temperature using the purely data driven approach by Wöhler et al. (2014). The derived temperature is used for the compensation of the thermal component and a set of reflectance properties is estimated. Based on these reflectance properties, a new temperature estimate is computed using the techniques from the previous section. This procedure is repeated using the current temperature estimate un-

til the result of the temperature estimation does not change significantly, i.e. the estimated temperature changes by less than 0.1 K. This final temperature estimate is then used to compute the reflectance for further analysis.

3.3. Reflectance normalization to standard geometry

For each M^3 pixel, the thermal emission spectrum given by the previously determined surface temperature is subtracted from the radiance spectrum. The resulting thermally corrected radiance spectrum is divided by the solar irradiance spectrum, which yields the thermally corrected reflectance spectrum. By employing the reflectance model of Hapke (1984, 2002), the spectrum of the single-scattering albedo is computed (this is in contrast to other normalization approaches, such as Besse et al. (2013), where an empirical photometric model is applied). The pixel-specific incidence and emission angle are inferred from the previously determined DEM and are then used to compute the reflectance spectrum for the standard illumination and viewing geometry of 30° incidence angle and 0° emission angle (Pieters et al., 2009). These normalized reflectance spectra are fully corrected with respect to the influences of surface temperature and small-scale topography. The spectral reflectance of the Boguslawsky region at a wavelength of 1579 nm is shown in Fig. 4.

3.4. Construction of spectral parameter maps

For the reflectance spectrum of each M^3 pixel, a continuum removal is performed by division by the convex hull (Fu et al., 2007). The continuum-removed spectra are used to determine spectral parameters characterizing the two prominent absorption bands near 1 μm and 2 μm. Specifically, for the 1 μm absorption band the width, relative depth, wavelength of minimum reflectance and continuum slope are determined. For the 2 μm absorption band, only the relative depth and the continuum slope are computed, due to the higher noise level than in the 1 μm range the band width and wavelength of minimum reflectance cannot be determined reliably. More details about the spectral parameter mapping are given by Wöhler et al. (2014).

The most important spectral parameter in the context of this work is the depth of the OH absorption band around 3 μm (since it is very difficult or impossible to distinguish between water and hydroxyl based on M^3 spectra, the abbreviation "OH" will denote "water and/or hydroxyl" in the following). As the M^3 spectral range does not cover the complete OH absorption band, the spectral ratio R_{2657}/R_{2817} (M^3 channels 77 vs. 81) and the integrated OH band depth were used to quantify the strength of the OH absorption band. The integrated OH band depth was computed in a manner similar to Clark et al. (2010): the continuum of the reflectance spectrum in the wavelength range of the OH absorption was approximated by a extrapolated straight line fitted to M^3 channels 74–77 (2537–2657 nm). The value of the ratio spectrum between the approximated continuum and the reflectance spectrum, subtracted from 1, was then integrated over M^3 channels 78–84 (2697–2936 nm). The value of this integral is called "integrated OH band depth" here.

In order to be able to observe temporal variations of the absorption depth, the spectral reflectances used to estimate the OH absorption depth are not computed based on all available M^3 images simultaneously but are determined for each individual M^3 image individually. Maps of the OH absorption depth are shown in Section 4.3 for the Boguslawsky region for lunar morning and midday.

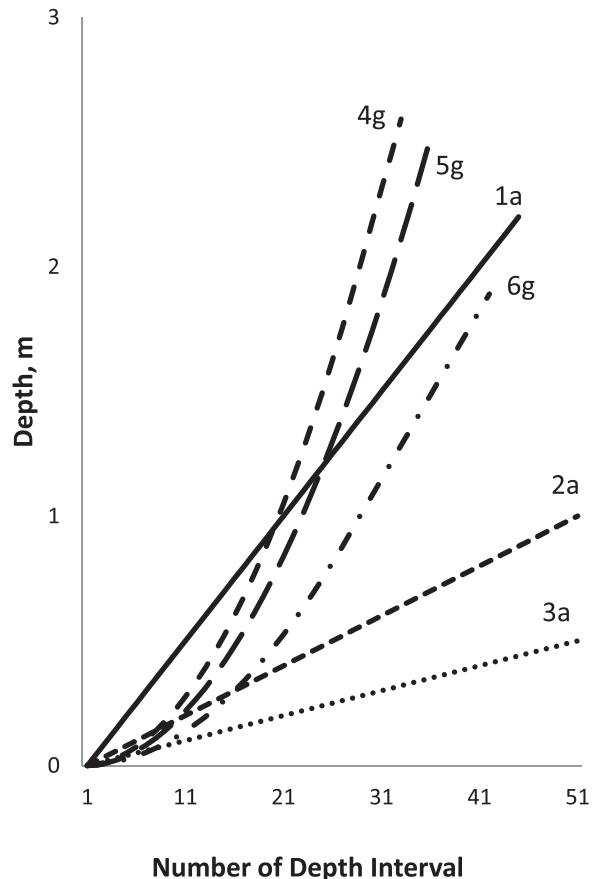


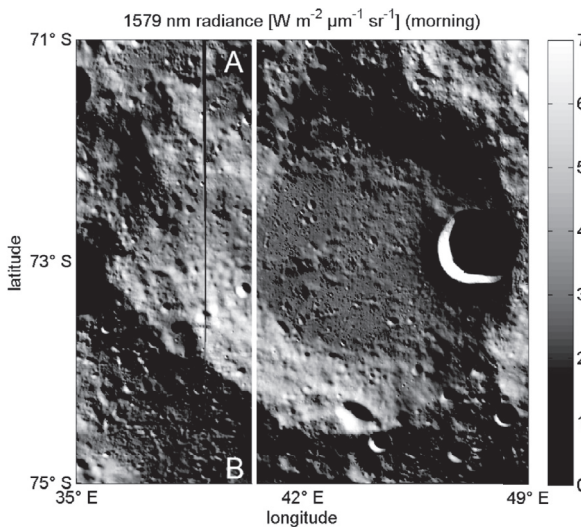
Fig. 6. Relationship between number of depth intervals and depth for different models.

4. Results obtained for the Boguslawsky region

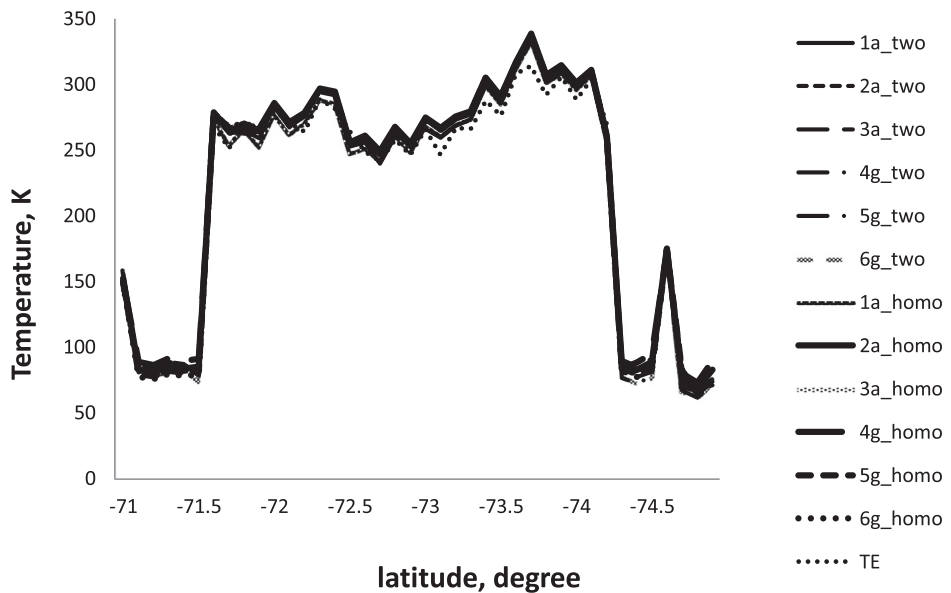
4.1. Temperature regime of crater Boguslawsky

The LOLA DEM of Fig. 5a shows that the average depth of the crater Boguslawsky is about 4.5 km from the flat bottom to the rim crest. The deepest point is located in the western part of the crater Boguslawsky D and reaches a depth of 5.5 km below the surrounding area. The surface slope and azimuthal orientation of the surface elements was derived from the LOLA DEM using the method of Zevenbergen and Thorne (1987). The crater bottom is flat (the slopes in this area do not exceed 5°–10°) (Fig. 5b). Some small hills are located in the western part of the bottom of crater Boguslawsky. The heights of these hills do not exceed 0.5 km relative to the crater floor. The slopes in this area are about 15°. Slope values on the walls of Boguslawsky vary from 10° to 40° with an average value of 30°. The maximal slopes are on the walls of crater Boguslawsky D, where the values reach 40°–60°. Fig. 5c shows the azimuthal orientation of the surface elements in the area of crater Boguslawsky.

In order to analyze the influence of time steps and depth steps on the modeled temperature of the lunar surface, we calculated the surface temperature of the part of crater Boguslawsky along the line AB (Fig. 7a) using the different time steps and six different depth steps for both models of the regolith properties (Fig. 7b–7e). Namely, steps along the solar azimuth were chosen as 1, 2, and 3°. For three studied models the depth steps were increased based on arithmetic progression (curves 1a, 2a, and 3a in Fig. 6), and for the other three models the depth steps were increased based on a parabolic function (curves 4g, 5g, and 6g in Fig. 6). The depth



(a) M^3 radiance image of crater Boguslawsky with studied line AB. Coordinates of points A and B are (71°S , 40.5°E) and (75°S , 40.5°E), respectively.



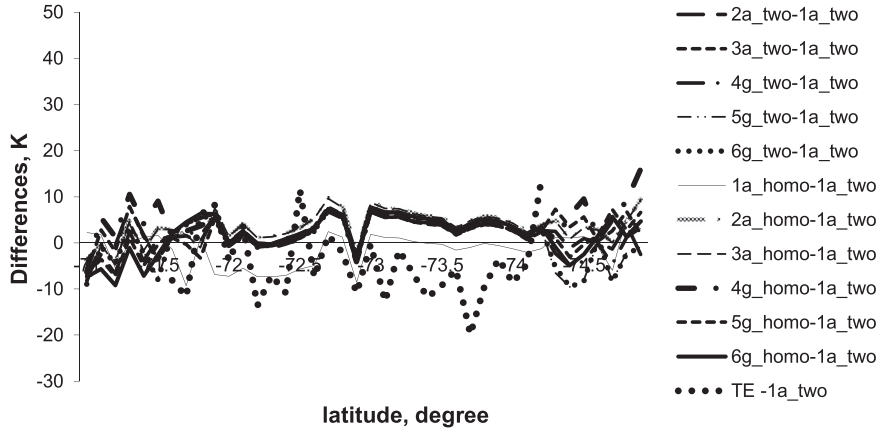
(b) Distribution of theoretical temperatures along the line AB in crater Boguslawsky for the acquisition time of the morning M^3 image (February 2, 2009, 6 h 44m 53s UT).

Fig. 7. Results of the different temperature estimation methods for the line AB shown in (a). Curves 1a_{two} – 6g_{two} represent the temperatures calculated using the two-layer model of the lunar surface structure for all depth intervals (see Fig. 6). The surface temperatures calculated using the homogeneous model of the lunar surface structure for all depth intervals is represented by the curves 1a_{homo} – 6g_{homo}. Results of the TE model are shown by the dotted curve.

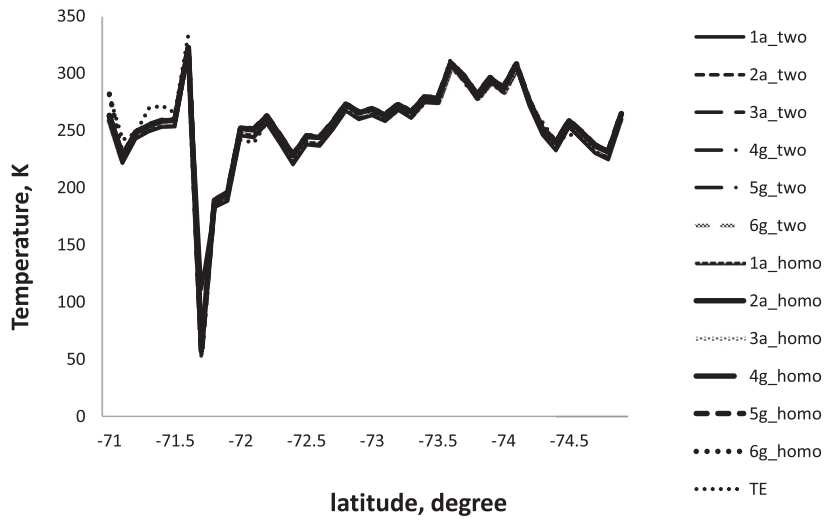
steps are equal to 5, 2, and 1 cm for curves 1a, 2a, and 3a, respectively.

Fig. 7b-e show the results of our calculations for different depth intervals (see Fig. 6) along the line AB (Fig. 7a) in the crater Boguslawsky at two time of M^3 image acquisition (February 2, 2009, 6 h 44 m 53 s UT (morning, local time is 8 h 24 m) and June 5, 2009, 16 h 36 m 36 s UT (midday, local time is 13 h 12 m). The differences between the calculated temperatures are shown in Fig. 7c and 7e. The temperatures calculated using the homogeneous model of the surface structure are generally higher than the temperatures calculated using the two-layer model of the surface structure. The average temperature difference between both lunar surface structure

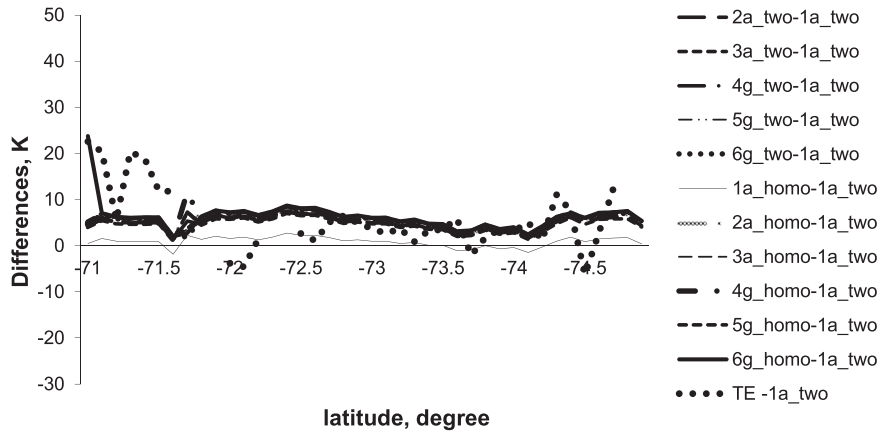
models is about 5 K. The highest differences (about 10 K) between both models are observed at temperatures below 130 K (Fig. 7c). They occur for shadowed regions with low temperatures, while the minimal differences are observed for warmer regions with temperatures above 250 K. Comparing different models, we have chosen the two-layer model with depth interval 4g (see Fig. 6) as the most suitable model for our calculations. The differences between the raytracing-based and the TE model are about 7 K for the illuminated regions of crater Boguslawsky. For regions with complex small topographic features the difference in spatial resolution of the DEMs used for the two modeling approaches can explain these temperature differences. The TE model cannot estimate the tem-



(c) Differences between simulated surface temperatures for different depth steps for both models of the surface structure for the acquisition time of the morning M³ image (February 2, 2009, 6h 44m 53s UT).



(d) Simulated temperatures along the line AB for lunar midday M³ image, acquired on June 5, 2009, 16h 36m 36s UT.



(e) Differences between simulated surface temperatures for different depth steps for both models of the surface structure for lunar midday M³ image acquired on June 5, 2009, 16h 36m 36s UT.

Fig. 7. Continued

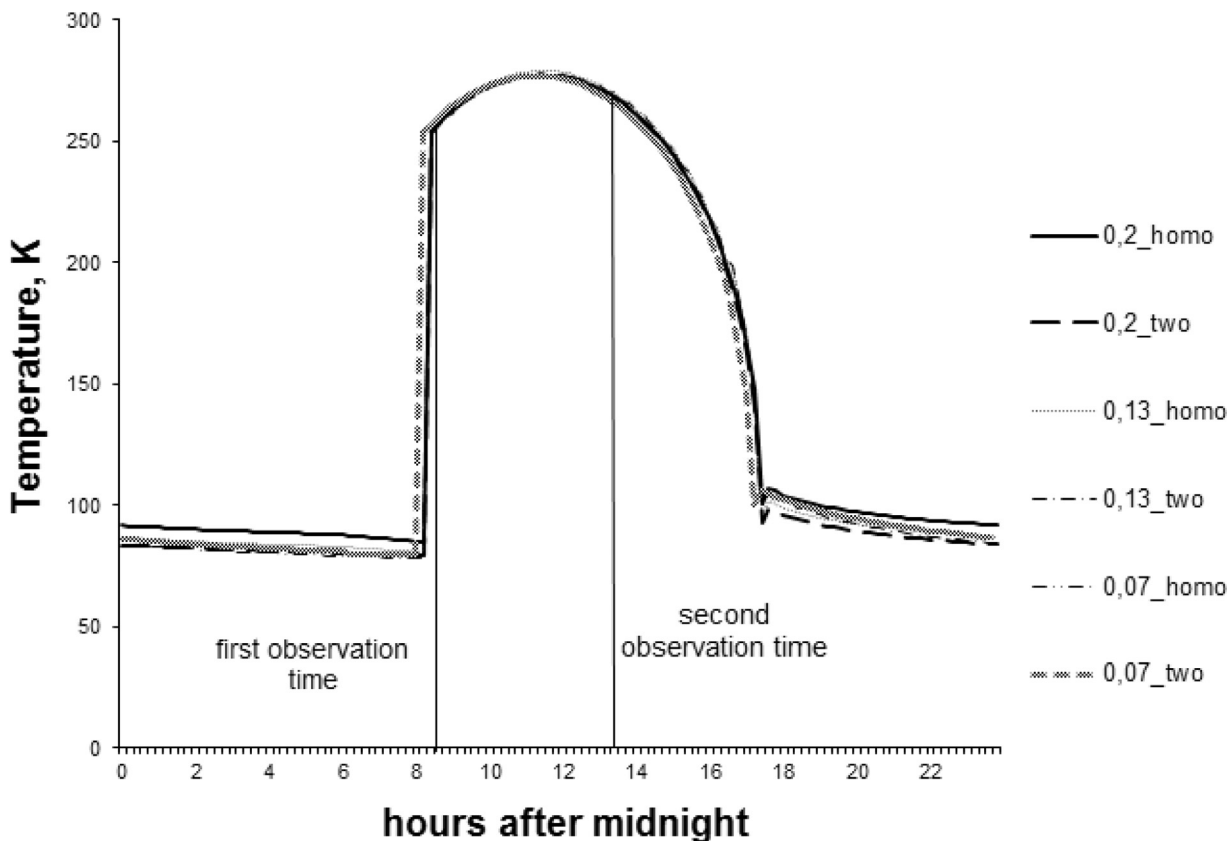


Fig. 8. Simulated surface temperature for the point with coordinates 73°S and 40.5°E in crater Boguslawsky for different time intervals. Curves annotated by “homo” denote the homogeneous surface structure model, curves annotated by “two” the two-layer surface structure model. The numbers indicate the time resolution in lunar hours used in the simulation. For example, the symbol “0.07_two” means two-layer surface structure model and time resolution of 0.07 lunar hours. Depth steps are taken from model 4g (see Fig. 6).

perature of shadowed regions and regions with low solar angle because for low solar irradiance the surface temperature is influenced by the thermal conductivity of the regolith despite its low value. For this reason, a comparison between both models only makes sense for regions with surface temperatures above 230 K.

The minimal difference between lunar surface temperatures calculated by using both surface structure models for all considered time intervals (0.07, 0.13, and 0.2 lunar hours) does not exceed 4 K and is observed during daytime, between 8 and 15 h after midnight. At the acquisition time of the M³ morning image, the differences between the simulated temperatures estimated using different time steps for both surface structure models do not exceed 1.5 K and are below 1.4 K at the acquisition time of the midday M³ image. Maximal differences are about 8.5 K during sunset and night, but at these moments in time M³ spectra of the lunar surface cannot be obtained. The small difference between results obtained with different time resolution means that even a time resolution of 0.2 lunar hours is appropriate for studies of the temperature regime of the lunar polar regions (Fig. 8).

In order to analyze the impact of the regolith infrared emissivity ε on the surface temperature, we used the values of emissivity from 0.94 to 0.97 with a step of 0.01. Differences between temperatures at the point with coordinates 73°S and 40.5°E located in the crater Boguslawsky are illustrated in Fig. 9, showing that the maximal differences between the temperatures for all values of surface emissivity are observed at daytime between 8 and 15 lunar hours after midnight. The difference reaches 2.3 K at about 6 h after midnight. Minimal differences are observed during the night and do not exceed 0.6 K.

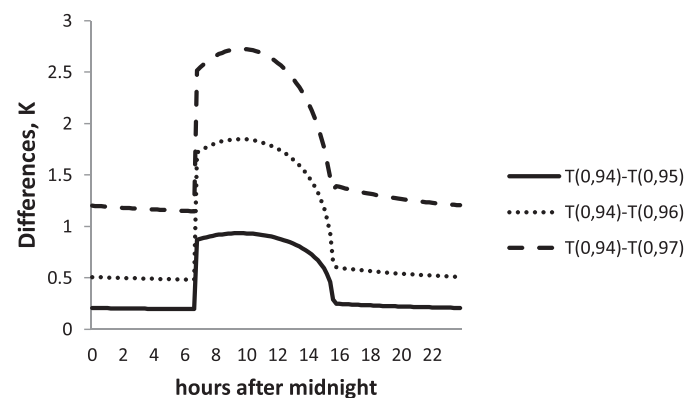


Fig. 9. Differences of simulated surface temperatures in the point with coordinates 73°S and 40.5°E as a function of emissivity. Symbols $T(0,94)$, $T(0,95)$, $T(0,96)$, and $T(0,97)$ mean surface temperatures, calculated with usage of $\varepsilon = 0.94$, 0.95, 0.96, and 0.97, respectively. Depth steps are taken from model 4g (see Fig. 6). Time resolution is 0.2 lunar hours.

The thermal equilibrium surface temperature estimation method described in Section 2.2 was used based on a set of M³ images of the crater Boguslawsky acquired at lunar morning (local time is 8 h 24 m) as well as a second set acquired shortly after lunar midday (local time is 13 h 12 m). These two sets were not acquired during the same lunation, but the illumination conditions are nearly identical within each set. Hence, we constructed a temperature map of the region for lunar morning and midday illumination, respectively, using the method described in

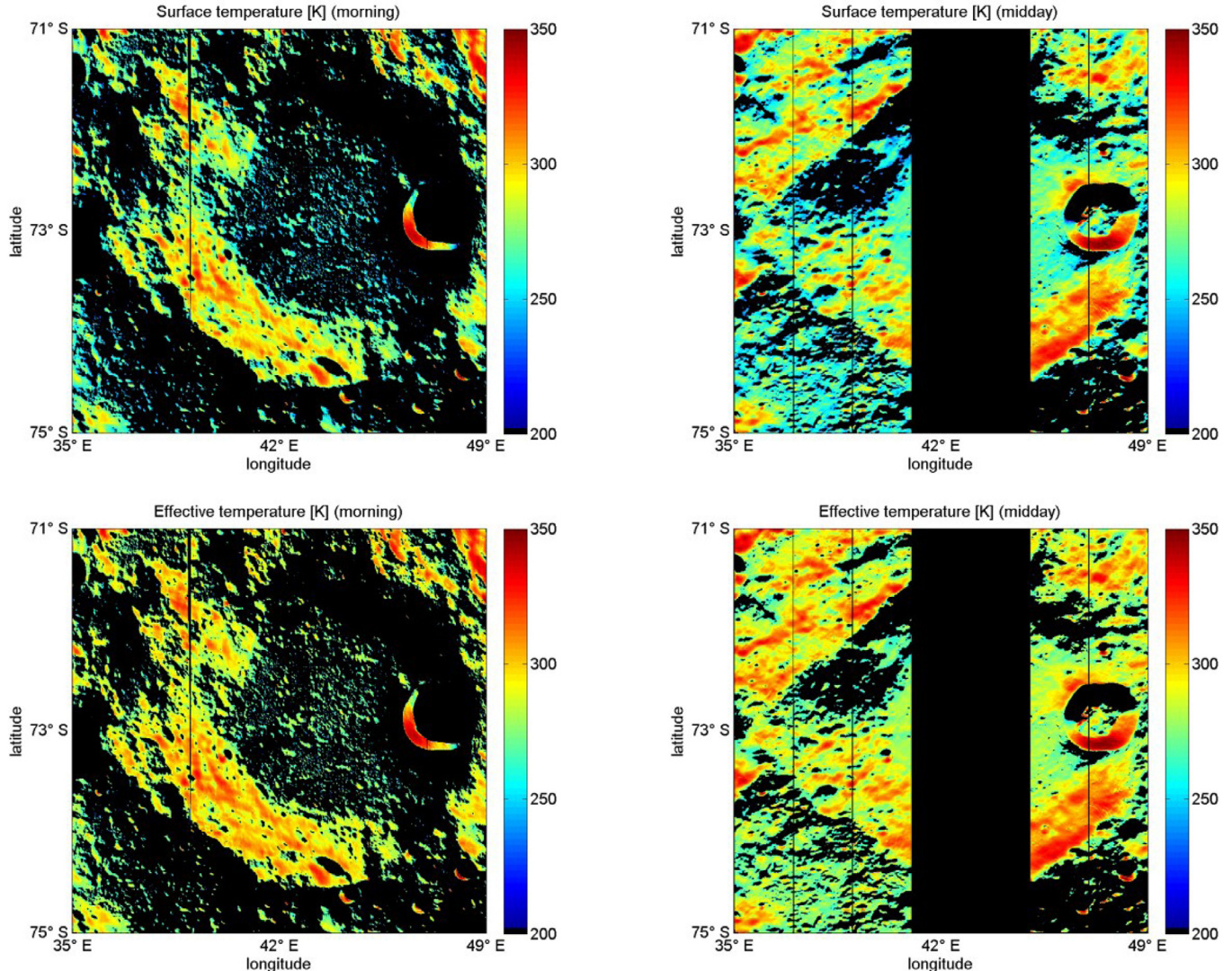


Fig. 10. Temperature maps of the Boguslawsky region obtained based on the TE method described in Section 2.2 under the assumption of a smooth surface (top row) and after taking into account the surface roughness according to Section 2.3 (bottom row) for lunar morning (left column) and midday (right column) illumination. Black denotes missing data or low signal-to-noise ratio due to low radiance.

Section 2.2 that assumes a smooth surface and the approach of Section 2.3 that takes into account the surface roughness (Fig. 10).

All temperature maps show the general trend that steeply illuminated surface parts are warmer than surface parts illuminated at low angles. The temperature of the crater floor is about 250 K in the morning and 270 K at midday, while the maximum temperature on the more steeply illuminated southern crater wall reaches 330 K both in the morning and at midday. The effective temperature obtained after taking into account the surface roughness always exceeds the temperature obtained under the assumption of a smooth surface (see Section 2.3).

In principle, the temperature regime in the Boguslawsky crater can also be studied using data of the Diviner instrument (Paige et al., 2010; Williams et al., 2017). However, the Diviner thermal infrared data yield channel-specific brightness temperatures which according to Bandfield et al. (2016) are strongly non-constant across the Diviner wavelength range for an incidence angle of 75° (as given around midday in the Boguslawsky region) (see also discussion in Section 2.1). Hence, the Diviner brightness temperatures are not directly comparable with the temperature values obtained by the raytracing-based and TE approaches described in Section 2.

4.2. Long-term thermal stability of volatile species in crater Boguslawsky

Let us consider the stability of volatile species during geological periods of time against thermal evaporation in crater Boguslawsky. The thermal stability of volatiles against evaporation is determined based on the maximal temperature during the lunar day. Results of calculations of the maximal temperature in the crater Boguslawsky using the raytracing-based model described in Section 2.1 are presented in Fig. 11.

As can be seen in Fig. 11, the maximal temperatures at the northern walls, floor and southern walls of crater Boguslawsky are about 200, 280, and 320 K, respectively. Such a strong difference in maximal temperatures may lead to different behavior of volatiles.

After the 2 km s⁻¹ LCROSS impact into a permanently shadowed region in the crater Cabeus near the south pole of the Moon, atoms of Ca, Hg, Mg (Gladstone et al., 2010) and Na (Killen et al., 2010) were detected in the impact-produced cloud above the impact site. The temperature in the LCROSS impact region was too low for release of Ca and Mg atoms to the lunar exosphere during thermal destruction of Ca and Mg containing silicates (Berezhnoy et al., 2012). For this reason, the appearance of these atoms in the

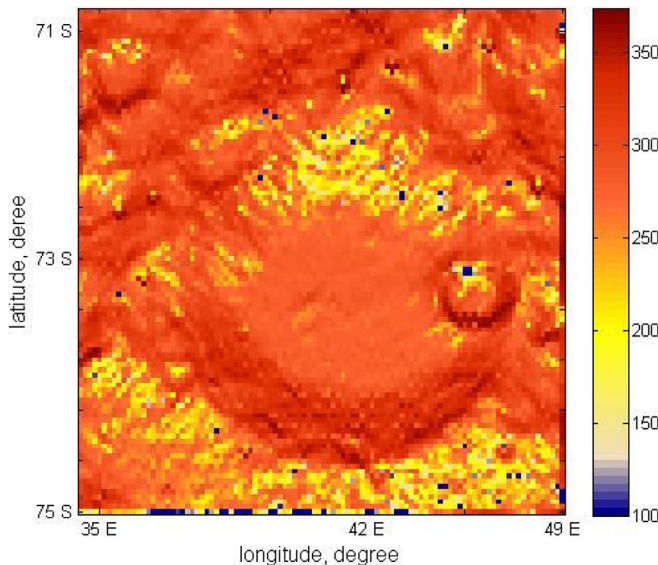


Fig. 11. Map of maximal surface temperatures of the Boguslawsky region. Depth steps are taken from 4g model (see Fig. 6). Time resolution is 0.2 lunar hours.

LCROSS impact-produced plume was explained by the presence of Ca, Hg, Mg, and Na atoms in lunar cold traps by Bereznay et al. (2012). Let us study the possibility of presence of these volatile species in the Boguslawsky crater region. The surface volatility temperature during geological periods of time is defined as the temperature of evaporation with a rate of about 10^{-12} m per year (Zhang and Paige, 2009) and is estimated as 132, 181, 226, 303, and 378 K for pure deposits of species Hg, S, Na, Mg and Ca, respectively (Bereznay et al., 2012). Comparing these volatility temperatures with the maximal temperatures in crater Boguslawsky, it is possible to determine regions of thermal stability of deposits of considered species. Namely, deposits of metal Ca can be found everywhere in the crater Boguslawsky. Surface deposits of metal Mg may exist on the floor and northern walls of crater Boguslawsky. Surface deposits of metal Na can be present only on the northern wall. Surface S and Hg deposits may also exist, but only in the coldest parts of the northern wall of crater Boguslawsky. Let us note that our estimation of areas of thermal stability of Hg, S, Na, Mg and Ca deposits is very preliminary, because it is based on the estimation of volatility temperatures for pure deposits of considered species. In reality Hg, S, Na, Mg, and Ca may not form pure deposits at the surface of the lunar regolith, but atoms of these elements may be connected with dust particles at the surface by chemical bonds, which may lead to significant changes in volatility temperature.

Special techniques need to be developed for the detection of predicted Hg, S, Na, Mg and Ca deposits in crater Boguslawsky. For example, an enrichment of S at the poles of the Moon may be detected by gamma-ray spectroscopy (Bereznay et al., 2003).

4.3. Temporal behavior of the OH absorption depth

The OH absorption depth maps shown in Fig. 12 indicate no significant qualitative differences between the R_{2657} / R_{2817} spectral ratio and the integrated OH band depth. The OH absorption depth is thus described in a similar way by the two proposed quantities.

As a general result, the strength of the OH absorption is higher in the morning than at midday. A comparison of Fig. 12 with Fig. 9 reveals an inverse correlation between surface temperature and OH absorption depth in the morning, while the temperature dependence disappears and is replaced by a largely uniform value of the OH absorption depth at midday. This behavior suggests that

OH-containing species may accumulate on the surface during the lunar night and almost disappear during the first half of the lunar day. Interestingly, a qualitatively similar behavior has been found by Grumpe et al. (2016) for the lunar farside crater Dryden located at low latitudes and observed under much steeper illumination conditions than crater Boguslawsky. In that work the surface roughness has not been taken into account, but according to Section 2.3 under those conditions surface roughness is a much less relevant factor for surface temperature estimation than it is for the oblique illumination conditions encountered in the lunar polar regions (similarly, Bandfield et al. (2016) show that the surface becomes increasingly isothermal with decreasing incidence angle). Hence, the observed temporal variations of the OH absorption band strength are presumably real and not just an artifact of roughness-related effects on the surface temperature estimation.

4.4. Short-term thermal stability of water/OH-containing species during the diurnal cycle in crater Boguslawsky

Based on the obtained information about the OH absorption feature, we can study the behavior of the surface water and/or OH-containing layer in the illuminated polar lunar regions in more details. The properties of the 3 μm absorption feature in the illuminated lunar polar regions were explained by the presence of a 0.09 μm thick OH-containing layer on the upper regolith layer with a typical particle size of about 1 μm (Pieters et al., 2009). The 3 μm absorption band was observed at the lunar morning and evening terminator by Sunshine et al. (2009), while theoretical modeling shows that diurnal migration of water molecules would result in an increased abundance at the morning terminator only (Schörgofer, 2014). Starukhina (2012) pointed out that the lunar exosphere would have a much higher density that the currently accepted upper bound if an amount of water sufficient to produce a spectral absorption band of variable strength over the lunar day was desorbed. Thus, additional studies of selected regions, observed at different moments in time including sunrise and sunset, are required for a deeper understanding of the origin of the 3 μm absorption feature on the Moon.

The evaporation of volatile species such as H_2O , Hg, S, Na, K, Mg, and Ca during the lunar day was studied using a model previously developed by Bereznay et al. (2012). The volatility temperature of species for such a short-term stability was determined as the temperature of evaporation of considered with a rate of about 10^{-5} m per year, corresponding to the evaporation of a 0.1 μm layer for three Earth days. This evaporation rate is reached for the considered species at a pressure of about 3×10^{-7} Pa. The short-term volatility temperature is estimated as 137, 198, 250, and 322 K for species H_2O , Hg, S, and Na, respectively. We can mention again as in Section 4.2 that these values of short-term volatility temperature, based on dependence of pressure on temperature for pure deposits of considered species, are very rough, because deposits of H_2O , Hg, S, and Na are mixed with the lunar regolith at the poles of the Moon. It leads to significant changes of volatility of such deposits in comparison with deposits consisted of pure species.

Let us compare the OH absorption band depth, indicated by the R_{2657} / R_{2817} spectral ratio, and surface temperature, estimated with usage of TE approach, for both available local times. For the morning one can see a constant OH absorption depth at surface temperatures lower than 270 K, while the OH absorption depth decreases in the range between 270–300 K and reaches a minimum at temperatures higher than 300 K (Fig. 12). This observed behavior of the OH absorption depth can be explained by evaporation of most of water and/or OH-containing molecules at 270–300 K. Our estimate shows that short-term surface water and/or OH-containing species are significantly less volatile than pure water ice deposits with an estimated short-term volatility tempera-

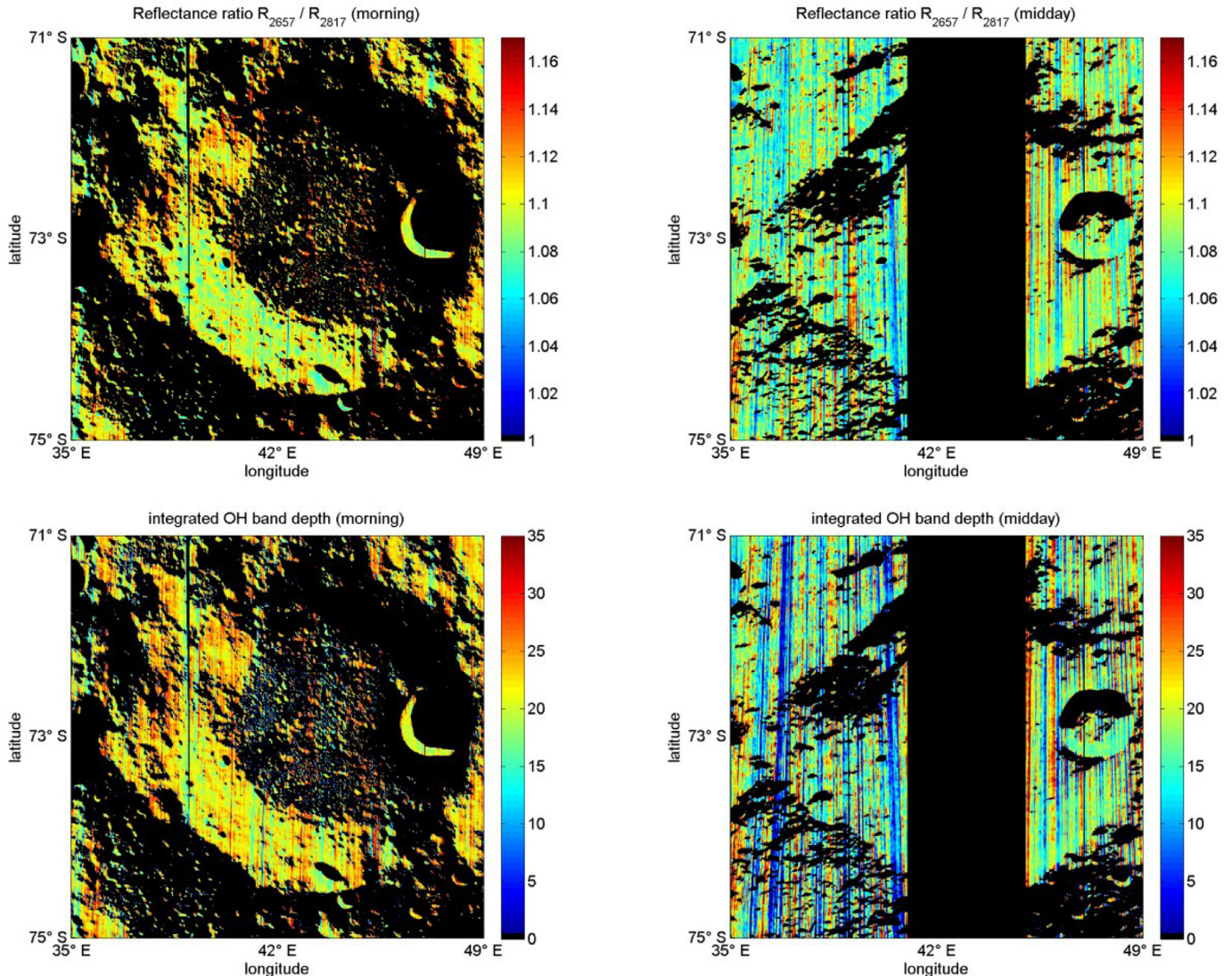


Fig. 12. The OH absorption depth as indicated by the spectral ratio R_{2657} / R_{2817} (top row) and by the integrated band depth (bottom row) in the morning (left) and at midday (right). Black denotes missing data or low signal-to-noise ratio due to low radiance.

ture of 137 K. It means that the volatility of these water and/or OH-containing species is between that of S and Na. Our results are consistent with measurements of the release of the main fraction of water and/or OH-containing species from studied lunar samples at 250–300 K in experiments performed by Poston et al. (2015). There is nearly no correlation between the OH absorption depth and surface temperature at midday (Fig. 12). This can be explained by ending of evaporation of water and/or OH-containing species by midday. In accordance with Poston et al. (2015) the thermal desorption of water and/or OH-containing species mainly occurs between sunrise and 10 h of local lunar time while the fraction of remaining non-desorbed volatiles increases with latitude and reaches about 20% at the latitude of crater Boguslawsky. The remaining non-desorbed hydrogen-containing volatiles are mainly in the form of hydroxyl, because water molecules typically desorb at temperatures below 350 K while hydroxyl desorbs at higher temperatures (Henderson, 2002).

We also consider the possibility of removal of a volatile-rich surface layer by solar photons. The integral solar flux $F_{\text{int}}(t_{\text{im}})$ for the considered region was calculated by integrating the solar flux between the time corresponding to 90° solar azimuth (sunrise) and the acquisition time of the M³ images (e.g. 129° for

the lunar morning M³ images) according to $F_{\text{int}}(t_{\text{im}}) = \int F(t) dt$. After that, the equivalent illumination time τ_{il} was estimated as $\tau_{\text{il}} = F_{\text{int}} / S_{\text{sun}}$, where $S_{\text{sun}} = 1367 \text{ W m}^{-2}$ is the solar constant. The remaining fraction F_{rem} of OH-containing volatiles was calculated as $F_{\text{rem}} = \exp(-\tau_{\text{il}}/\tau_{\text{photo}})$, where τ_{photo} is the photolysis lifetime of OH-containing species in the upper layer of the lunar regolith. The photolysis lifetime value for surface OH-containing molecules is not a unique value because it strongly depends on the binding energy between the OH radical and the grid of the surface dust particles. In our case it was assumed to be 22 hours, the value of the photolysis lifetime of gas-phase water molecules (Huebner et al., 1992). This value is close to the experimental value of the photodesorption lifetime of water molecules for average solar activity at the sub-solar point on the Moon equal to 14 h (Mitchell et al., 2013). Due to the long computation time, the calculations of the remaining fraction of OH-containing species could only be performed for the line AB indicated in Fig. 5a.

There is no correlation ($r^2 = -0.056$) between the R_{2657} / R_{2817} spectral ratio and the remaining fraction of OH-containing species in the morning (Fig. 14). Changing the photolysis lifetime to 5 and 100 h leads to changes of the r^2 value only to -0.072 and -0.051 , respectively. This means that the photolysis of OH-

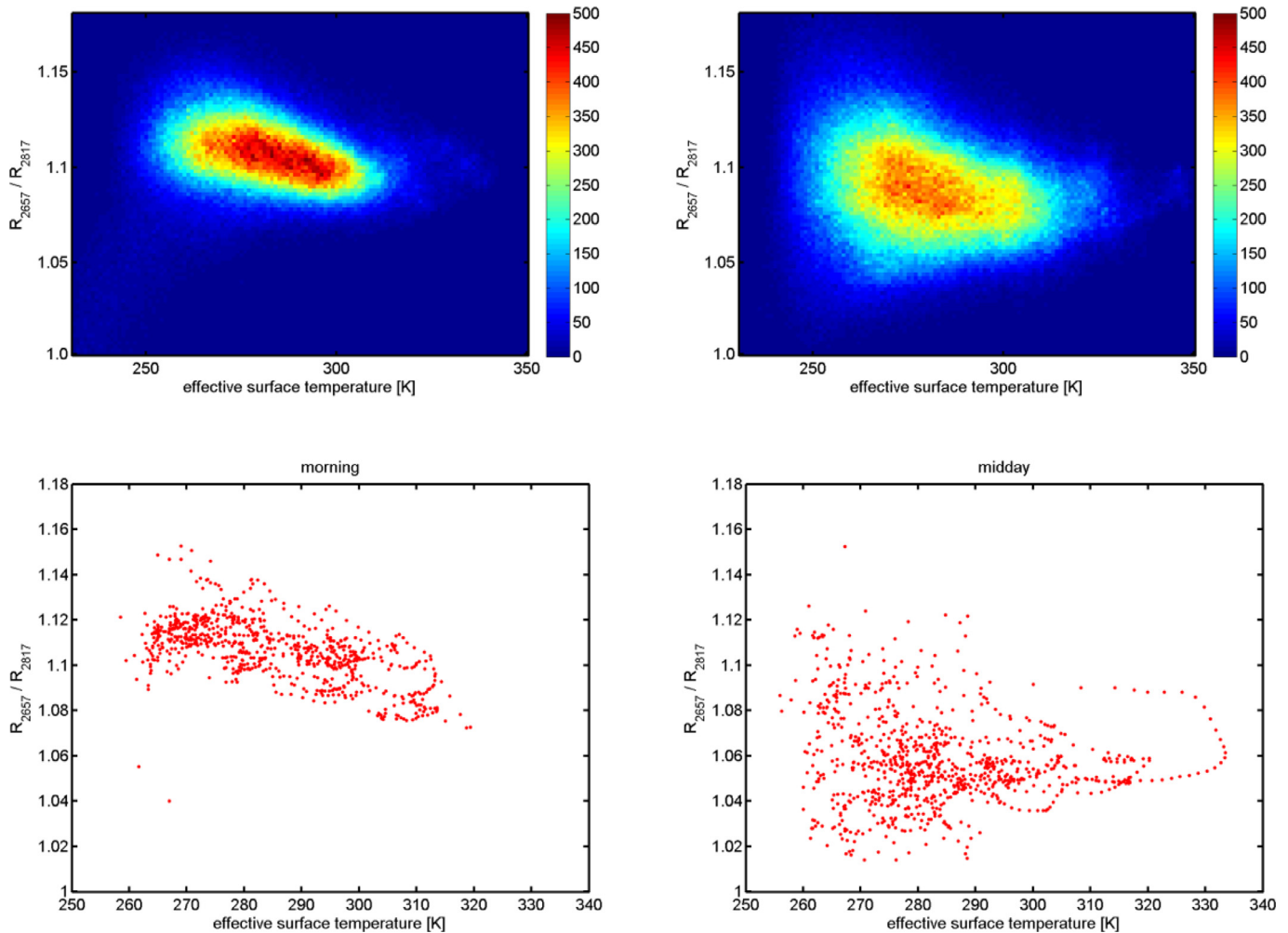


Fig. 13. Density plot depicting the dependence of the OH absorption band depth on surface temperature for the whole crater Boguslawsky (35° E– 49° E, 71° S– 75° S) (density plots, top row) and for the line AB (scatter plots, bottom row) for morning (left column) and mid-day (right column) M^3 images.

containing species at any realistic value of the photolysis lifetime of these species cannot explain the obtained observational data and that thermal evaporation is the main mechanism of removal of surface OH-containing species soon after sunrise. Our results are in agreement with the conclusions of Poston et al. (2015) regarding thermal evaporation as a main mechanism of removal of OH-containing lunar surface volatiles. A weak correlation between the R_{2657}/R_{2817} spectral ratio and remaining fraction of OH-containing species at midday is detected, where $r^2 = 0.47$ (Fig. 14), while for this local time there is a weaker correlation between the R_{2657}/R_{2817} spectral ratio and the effective surface temperature than in the morning (see Fig. 13, where the similarity between the correlation plots of the whole region and the line AB, respectively, indicates that the behavior observed for the line AB is representative of the whole region). This means that photolysis by solar photons is likely the main mechanism of removal of remnants of OH-containing species during midday.

Let us note that the quality of the M^3 data used is not high enough for an accurate estimation of the typical photolysis lifetime of surface OH-containing species in the illuminated lunar polar regions. The infrared spectrometer LIS on board the planned Russian Luna-Glob mission will study the water and OH behavior in the illuminated lunar polar regions with high spatial and temporal resolution (Mantsevich et al., 2015), which will help to achieve a deeper understanding of the behavior of water and OH-containing species on the Moon.

5. Summary and conclusion

In this work we have examined the lunar crater Boguslawsky as a typical region in the southern lunar highlands with regard to its temperature regime and the dependence of the depth of the OH-related absorption band near $3\mu\text{m}$ wavelength on the surface temperature and the local daytime. We have compared two methods for estimating the lunar surface temperature. One method relies on a raytracing and simulation of thermal diffusion approach, while the other method is based on the assumption of thermal equilibrium, utilizing M^3 spectral reflectance data for estimating the amount of absorbed solar energy. The surface roughness has been taken into account in the surface temperature estimation. The results of these two surface temperature estimation methods differ by not more than a few K. A comparison between the volatility temperatures of species Hg, S, Na, Mg, and Ca with the maximal surface temperatures has permitted to determine regions in which these volatile species could form stable deposits. Furthermore, we found that the OH absorption depth is higher at lunar morning than at lunar midday, where at lunar morning constant OH absorption depth is detected at temperatures lower than 270 K, while the OH absorption depth decreases in the range between 270 and 300 K and reaches a minimum at temperatures higher than 300 K. These observational facts can be explained by accumulation of $\text{H}_2\text{O}/\text{OH}$ -containing species on the surface during the lunar night and a disappearance during the first half of the lunar day by thermal evap-

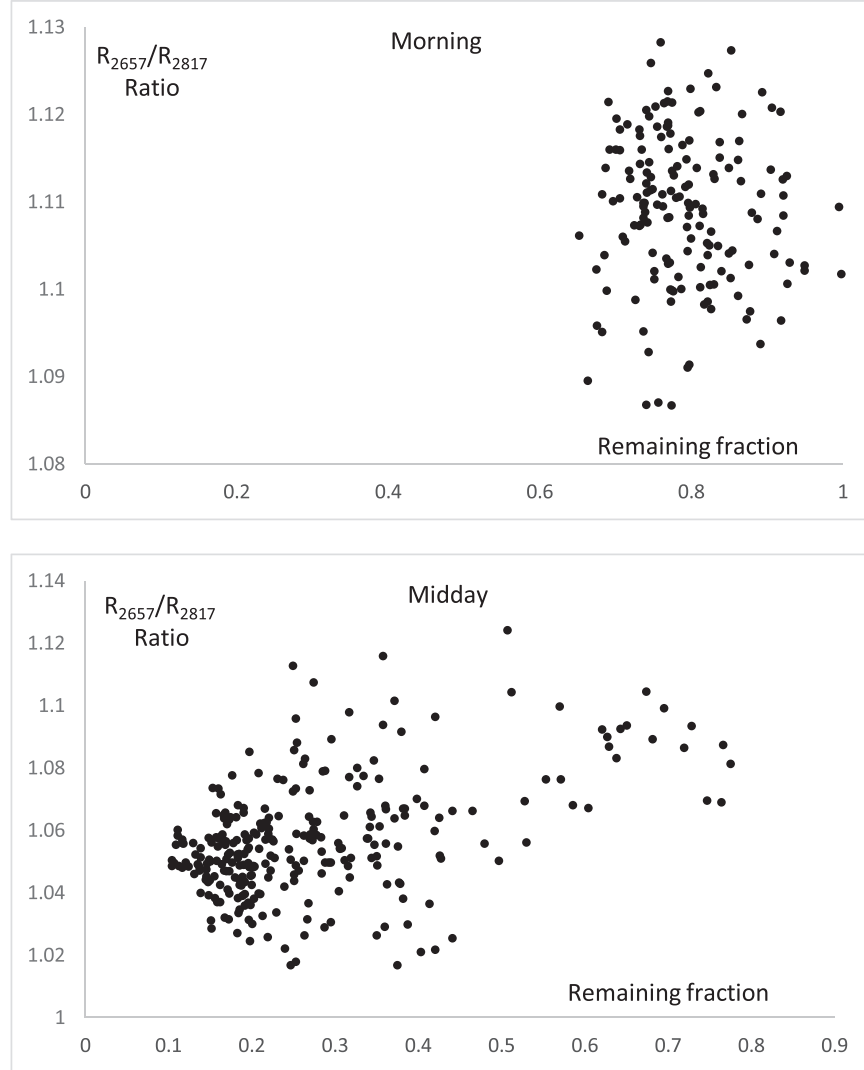


Fig. 14. Dependence of the OH absorption band depth, indicated as the R_{2657}/R_{2817} ratio, on the calculated remaining fraction of OH-containing volatiles for the morning (top) and midday (bottom) M^3 image along the line AB in crater Boguslawsky. Photolysis lifetime is equal to 22 h.

oration of these species. The lack of correlation between OH absorption depth and theoretical remaining fraction of OH-containing species in the morning indicates that the water molecules and/or OH-containing species are removed mainly by thermal evaporation soon after sunrise. At midday, the OH absorption depth increases with increasing remaining fraction of OH-containing species, suggesting that photolysis by solar photons is the main mechanism that removes remnants of OH-containing species later in the lunar day.

Acknowledgments

A.A.B., E.A.F., and V.V.S. were supported by RFBR-DFG grant No. 15-52-12369. C.W. and A.G. were supported by RFBR-DFG grant No. WO 1800/7-1.

Appendix A. Generation of Gaussian random surfaces

The generation of Gaussian random surfaces is based on the algorithm by [Muinonen and Saarinen \(2000\)](#) which was also used by [Lagerros \(1998\)](#). The Gaussian surface $z = z(x, y)$ is specified by the height deviation from the mean plane. The roughness may be described by the correlation function $C_z(\xi, \eta)$ where $\xi = x_1 - x_2$ and

$\eta = y_1 - y_2$ are the difference in the horizontal and the vertical coordinate, respectively, between any two points on the surface. The surface is assumed to have a Gaussian correlation function

$$C_z = \exp(-(\xi^2 + \eta^2)/2l_z^2) \quad (A1)$$

where l is the correlation length. It is convenient to describe the surface z in terms of a two-dimensional Fourier-series representation

$$z(x, y) = \sum_{p=-\infty}^{\infty} \sum_{q=-\infty}^{\infty} Z_{pq} \exp(i(pK_{FT}x + qK_{FT}y)) \quad (A2)$$

and the correlation function in terms of the two-dimensional cosine series

$$C_z(\xi, \eta) = \sum_{p=0}^{\infty} \sum_{q=0}^{\infty} c_{pq} \cos(pK_{FT}\xi) \cos(qK_{FT}\eta), \quad (A3)$$

where $K_{FT} = \pi/L_z$. Here, $2L_z$ is the period of the surface, i.e. the surface is assumed to be periodically repeated outside of the modeled surface area and $2L_z$ is the edge length of the quadratic surface area. In case of a rectangular area, the values of K_{FT} differ for the vertical and the horizontal direction, respectively and need to be

modified accordingly. The cosine coefficients of C_z are given by

$$c_{pq} = \frac{\pi\kappa^2}{2}(2 - \delta_{0p})(2 - \delta_{0q}) \exp(-\pi^2\kappa^2(p^2 + q^2)/2) \quad (\text{A4})$$

where $\kappa_z = l_z/L_z$ and δ_{ij} is the Kronecker delta function.

From the assumption that C_z is the correlation function of z follows that Z_{pq} are normally distributed with zero mean and standard deviation σ_z if the variance of the real and imaginary parts of Z_{pq} , respectively, are given by

$$\text{Var}(\text{Re}(Z_{pq})) = \frac{1}{8}(1 + \delta_{p0} + \delta_{q0} + 5\delta_{p0}\delta_{q0})c_{pq}\sigma_z^2 \text{ and} \quad (\text{A5})$$

$$\text{Var}(\text{Im}(Z_{pq})) = \frac{1}{8}(1 + \delta_{p0} + \delta_{q0} - 3\delta_{p0}\delta_{q0})c_{pq}\sigma_z^2. \quad (\text{A6})$$

The roughness of the surface, i.e. the RMS slope, is given by $s_{\text{rough}} = \sigma_z/l_z$.

Since z is real valued, the real part of its Fourier series coefficients is required to be an even function and the imaginary part of its Fourier series coefficients is required to be an odd function, i.e. $\text{conj}(Z_{p,-q}) = Z_{pq}$ where conj denotes the complex conjugate. Furthermore, z is supposed to be mean free and thus $Z_{00} = 0$. A necessary and sufficient set of Fourier series coefficients is thus given by Z_{pq} for $p \geq 0$ and $-\infty < q < \infty$.

The correlation function is a Gaussian, its series coefficients tend to zero and thus a finite set of coefficients is sufficient if the correlation length l_z is small compared to the period $2L_z$. Therefore, Gaussian random surfaces are conveniently generated by sampling a set of Fourier series coefficients and applying the inverse Fast Fourier Transform.

References

- Arnold, J.R., 1979. Ice in the lunar polar regions. *J. Geophys. Res.* 84 (B10), 5659–5668. doi:10.1029/JB084iB10p05659.
- Bandfield, J.L., Edwards, C.S., Poston, M.J., Klima, R.L., 2016. Lunar H₂O/OH distributions: revised infrared spectra from improved thermal corrections. *Lunar and Planetary Science Conference* 47 abstract No. 1594.
- Berezhnoi, A.A., Klumov, B.A., 1998. Lunar ice: can its origin be determined? *J. Exper. Theor. Physics Lett.* 68 (2), 163–167. doi:10.1134/1.567840.
- Berezhnoi, A.A., Hasebe, N., Hiramoto, T., Klumov, B.A., 2003. Possibility of the presence of S, SO₂, and CO₂ at the poles of the Moon. *Publ. Astron. Soc. Japan* 55 (4), 859–870. doi:10.1093/pasj/55.4.859.
- Berezhnoi, A.A., Kozlova, E.A., Sinitsyn, M.P., Shangaraev, A.A., Shevchenko, V.V., 2012. Origin and stability of lunar polar volatiles. *Adv. Sp. Res.* 50 (12), 1638–1646. doi:10.1016/j.asr.2012.03.019.
- Birkebak, R.C., 1972. Spectral reflectance and emittance of Apollo 11 and 12 lunar material. *Amer. Inst. Aerona. Astronau. J.* 10, 1064–1067. doi:10.2514/3.50295.
- Besse, S., Sunshine, J., Staid, M., Boardman, J., Pieters, C., Guasqui, P., Malaret, E., McLaughlin, S., Yokota, Y., Li, J.-Y., 2013. A visible and near-infrared photometric correction for Moon mineralogy mapper M³. *Icarus* 222 (1), 229–242. doi:10.1016/j.icarus.2012.10.036.
- Boyce, J.W., Liu, Y., Rossman, G.R., Guan, Y., Eiler, J.M., Stolper, E.M., Taylor, L.A., 2010. Lunar apatite with terrestrial volatile abundances. *Nature* 466 (7305), 466–469. doi:10.1038/nature09274.
- Carruba, V., Coradini, A., 1999. Lunar cold traps: effects of double shielding. *Icarus* 142, 402–413.
- Clark, R.N., et al., 2009. Detection of adsorbed water and hydroxyl on the Moon. *Science* 326 (5952), 562–564. doi:10.1126/science.1178105.
- Clark, R.N., et al., 2010. Water and hydroxyl on the Moon as seen by the Moon Mineralogy Mapper (M³). *Lunar and Planetary Science Conference* 41 abstract No. 2302.
- Clark, R.N., Pieters, C.M., Green, R.O., Boardman, J.W., Noah, E.P., 2011. Thermal removal from near-infrared imaging spectroscopy data of the Moon. *J. Geophys. Res.* 116, E00G16. doi:10.1029/2010E003751.
- Colaprete, A., et al., 2010. Detection of Water in the LCROSS Ejecta Plume. *Science* 330 (6003), 463–468. doi:10.1126/science.1186986.
- Crider, D.H., Vondrak, R.R., 2000. The solar wind as a possible source of lunar polar hydrogen deposits. *J. Geophys. Res.* 105, 26773–26782.
- Davidson, B.J.R., et al., 2015. Interpretation of thermal emission. I. The effect of roughness for spatially resolved atmosphereless bodies. *Icarus* 252, 1–21.
- Feldman, W.C., Maurice, S., Binder, A.B., Barracough, B.L., Elphic, R.C., Lawrence, D.J., 1998. Fluxes of fast and epithermal neutrons from lunar prospector: evidence for water ice at the lunar poles. *Science* 281, 1496–1500.
- Fu, Z., Robles-Kelly, A., Caelli, T., Tan, R.T., 2007. On automatic absorption detection for imaging spectroscopy: a comparative study. *IEEE Trans. Geosci. Remote Sens.* 45, 3827–3844.
- Gladstone, G.R., et al., 2010. LRO-LAMP observations of the LCROSS impact plume. *Science* 330 (6003), 472–476. doi:10.1126/science.1186474.
- Greenhagen, B.T., Paige, D.A., 2006. Mapping lunar surface petrology using the mid-infrared emissivity maximum with the LRO diviner radiometer. In: *Lunar and Planetary Science Conference* 37, p. 2046.
- Grumpe, A., Belkhir, F., Wöhler, C., 2014. Construction of lunar DEMs based on reflectance modelling. *Adv. Sp. Res.* 54 (10), 2029–2040. doi:10.1016/j.asr.2013.07.030.
- Grumpe, A., Wöhler, C., 2014. Recovery of elevation from estimated gradient fields constrained by digital elevation maps of lower lateral resolution. *ISPRS J. Photogram. Remote Sens.* 94, 37–54. doi:10.1016/j.isprsjprs.2014.04.11.
- Grumpe, A., Wöhler, C., Berezhnoy, A.A., Feoktistova, E.A., Evdokimova, N.A., Kapoor, K., Shevchenko, V.V., 2016. Illumination dependent behavior of the lunar 3 μm absorption band depth in the lunar crater Dryden. In: *Proc. 7th Moscow Solar System Symposium*. Moscow, Russia abstract No. 7MS3-PS-26.
- Grumpe, A., Zirin, V., Wöhler, C., 2015. A normalisation framework for (hyper-) spectral imagery. *Planet. Sp. Sci.* 111, 1–33. doi:10.1016/j.pss.2014.10.013.
- Hapke, B., 1981. Bidirectional reflectance spectroscopy. I. Theory. *J. Geophys. Res.* 86, 3039–3054. doi:10.1029/JB086iB04p03039.
- Hapke, B., 1984. Bidirectional reflectance spectroscopy: 3. Correction for macroscopic roughness. *Icarus* 59, 41–59. doi:10.1016/0019-1035(84)90054-X.
- Hapke, B., 2002. Bidirectional reflectance spectroscopy: 5. The coherent backscatter opposition effect and anisotropic scattering. *Icarus* 157, 523–534. doi:10.1006/icar.2002.6853.
- Hapke, B., 2005. *Theory of Reflectance and Emittance Spectroscopy*. Cambridge Univ. Press, New York.
- Hapke, B., 2012. *Theory of reflectance and emittance spectroscopy*, second ed. Cambridge University Press, Cambridge, UK.
- Hauri, E.H., Saal, A.E., Rutherford, M.J., Van Orman, J.A., 2015. Water in the Moon's interior: truth and consequences. *Earth Planet. Sci. Lett.* 409, 252–264. doi:10.1016/j.epsl.2014.10.053.
- Hayne, P.O., Hendrix, A., Sefton-Nash, E., Siegler, M.A., Lucey, P.G., Rutherford, K.D., Williams, J.-P., Greenhagen, B.T., Paige, D.A., 2015. Evidence for exposed water ice in the Moon's south polar regions from lunar reconnaissance orbiter ultraviolet albedo and temperature measurements. *Icarus* 255, 58–69. doi:10.1016/j.icarus.2015.03.032.
- Helfenstein, P., Shepard, M.K., 1999. Submillimeter-scale topography of the lunar regolith. *Icarus* 141, 107–131.
- Henderson, M.A., 2002. The interaction of water with solid surfaces: fundamental aspects revisited. *Surf. Sci. Rep.* 46 (1–8), 1–308. [http://dx.doi.org/10.1016/s0167-5729\(01\)00020-6](http://dx.doi.org/10.1016/s0167-5729(01)00020-6).
- Horn, B.K.P., 1990. Height and gradient from shading. *Int. J. Comput. Vision* 5 (1), 37–75.
- Huebner, W.F., Keady, J.J., Lyon, S.P., 1992. Solar photo rates for planetary atmospheres and atmospheric pollutants. *Astrophys. Sp. Sci.* 195 (1), 291–294 1–289.
- Ivanov, M.A., et al., 2014. Geological context of potential landing site of the Luna-Glob mission. *Solar Syst. Res.* 48 (6), 391–402. doi:10.1134/S0038094614060021.
- Ivanov, M.A., Basilevsky, A.T., Abdralkhimov, A.M., Karachevtseva, I.P., Kokhanov, A.A., Head, J.W., 2015a. Crater Boguslawsky on the Moon: geological structure and an estimate of the degree of rockiness of the floor. *Solar Syst. Res.* 49 (7), 367–382. doi:10.1134/S0038094615060039.
- Ivanov, M.A., Hiesinger, H., Abdralkhimov, A.M., Basilevsky, A.T., Head, J.W., Pasckert, J.-H., Bauch, K., van der Bogert, C.H., Gläser, P., Kohanov, A., 2015b. Landing site selection for Luna-Glob mission in crater Boguslawsky. *Planet. Space Sci.* 117, 45–63. doi:10.1016/j.pss.2015.05.007.
- Keihm, S.J., Langseth, M.G., 1973. Surface brightness temperatures at the Apollo 17 heat flow site: thermal conductivity of the upper 15 cm of regolith. In: *Proceedings of Lunar and Planetary Science Conference*, 5, pp. 2503–2513.
- Killen, R.M., et al., 2010. Observations of the lunar impact plume from the LCROSS event. *Geophys. Res. Lett.* 37 CiteID L23201.
- Lagerros, J.S.V., 1998. Thermal physics of asteroids – IV. Thermal infrared beaming. *Astron. Astrophys.* 332, 1123–1132.
- Langseth, M.G., Keihm, S.J., Peters, K., 1976. Revised lunar heat-flow values. In: *Proceedings of Lunar Planetary Science Conference*, 7, pp. 3143–3171.
- Ledlow, M.J., Burns, J.O., Gisler, G.R., Zhao, J.-H., Zelik, M., Baker, D.N., 1992. Subsurface emissions from Mercury: VLA radio observations at 2 and 6 centimeters. *Astrophys. J.* 384, 340–355.
- Li, S., Milliken, R.E., 2016. An empirical thermal correction model for Moon mineralogy mapper data constrained by laboratory spectra and diviner temperatures. *J. Geophys. Res.* 121. doi:10.1002/2016JE005035.
- Linsky, J.L., 1966. Models of the lunar surface including temperature-dependent thermal properties. *Icarus* 5, 606–634.
- Litvak, M.L., et al., 2012. Global maps of lunar neutron fluxes from the LEND instrument. *J. Geophys. Res.* 117 (E12), E00H22.
- Lucas, J.W., Conel, J.E., Hagemeyer, W.A., Garipay, R.R., Saari, J.M., 1967. Lunar surface thermal characteristics from Surveyor 1. *J. Geophys. Res.* 72, 779–789.
- Mantsevich, S.N., Korablev, O.I., Kalinnikov, Yu.K., Ivanov, A.Yu., Kiselev, A.V., 2015. Wide-aperture TeO₂ AOTF at low temperatures: operation and survival. *Ultrasonics* 59, 50–58.
- McCord, T.B., Taylor, L.A., Combe, J.-P., Kramer, G., Pieters, C.M., Sunshine, J.M., Clark, R.N., 2011. Sources and physical processes responsible for OH/H₂O in the lunar soil as revealed by the Moon mineralogy mapper (M³). *J. Geophys. Res.* 116 (E6), E00G05. doi:10.1029/2010JE003711.
- McClanahan, T.P., et al., 2015. Evidence for the sequestration of hydrogen-bearing volatiles towards the Moon's southern pole-facing slopes. *Icarus* 255, 88–99.

- McKay, D.S., Heiken, G., Basu, A., Blanford, G., Simon, S., Reedy, R., French, B.M., Papike, J., 1991. The lunar regolith. In: Heiken, G.H., Vaniman, D.T., French, B.M. (Eds.), *Lunar Sourcebook. A User's Guide to the Moon*. Cambridge Univ. Press, pp. 357–474.
- Mitchell, E.H., Raut, U., Fulvio, D., Schaible, M.J., Dukes, C.A., Baragiola, R.A., 2013. Ultraviolet photodesorption as a driver of water migration on the lunar surface. *Planet. Sp. Sci.* 89, 42–46. doi:10.1016/j.pss.2013.02.002.
- Mitrofanov, I.G., Shevchenko, V.V., Sanin, A.B., Boynton, W.V., Chin, G., Garvin, J.B., Golovin, D., Evans, L.G., Harshman, K., Kozyrev, A.S., Litvak, M.L., Malakhov, A., Mazarico, E., Milikh, T., McClanahan, G., Mokrousov, M., Nandikotkur, G., Neumann, G.A., Nuzhdin, I., Shvetsov, R., Sagdeev, V., Smith, D.E., Starr, R., Tretyakov, V.I., 2010a. Lunar exploration neutron detector for the NASA lunar reconnaissance. *Space Sci. Rev.* 150, 183–207.
- Mitrofanov, I.G., Shevchenko, V.V., Sanin, A.B., Boynton, W.V., Chin, G., Garvin, J.B., Golovin, D., Evans, L.G., Harshman, K., Kozyrev, A.S., Litvak, M.L., Malakhov, A., Mazarico, T., McClanahan, E., Milikh, G., Mokrousov, M., Nandikotkur, G., Neumann, G.A., Nuzhdin, I., Shvetsov, R., Sagdeev, V., Smith, D.E., Starr, R., Tretyakov, V.I., Trombka, J., Usikov, D., Varenkov, A., Vostrukhin, A., Zuber, M.T., 2010b. Hydrogen mapping of the lunar South Pole using the LRO neutron detector experiment LEND. *Science* 330 (6003), 483–486.
- Mitrofanov, I., Litvak, M., Sanin, A., Malakhov, A., Golovin, D., Boynton, W., Droege, G., Chin, G., Evans, L., Harshman, K., Fedosov, F., Garvin, J., Kozyrev, A., McClanahan, T., Milikh, G., Mokrousov, M., Starr, R., Sagdeev, R., Shevchenko, V., Shvetsov, V., Tret'yakov, V., Trombka, J., Varenkov, A., Vostrukhin, A., et al., 2012. Testing polar spots of water-rich permafrost on the Moon: LEND observations onboard LRO. *J. Geophys. Res.* 117 (E12), E00H27.
- Muinonen, K., Saarinen, K., 2000. Ray optics approximation for Gaussian random cylinders. *J. Quant. Spectroscop. Rad. Transf.* 64, 201–218.
- Neumann, G.A. Lunar reconnaissance orbiter lunar orbiter laser altimeter reduced data record and derived products software interface specification version 2.6..
- Nicodemus, F.E., 1965. Directional reflectance and emissivity of an opaque surface. *Appl. Optics* 4, 767–773.
- Nozette, S., Lichtenberg, C.L., Spudis, P., Bonner, R., Ort, W., Malaret, E., Robinson, M., Shoemaker, E.M., 1996. The clementine bistatic radar experiment. *Science* 274 (5292), 1495–1498.
- Ong, L., Asphaug, E., Korycansky, D., Coker, R.F., 2010. Volatile retention from cometary impacts on the Moon. *Icarus* 207, 578–589.
- Paige, D.A., et al., 2010. Diviner lunar radiometer observations of cold traps in the Moon's South Polar region. *Science* 330, 479–482.
- Piddington, J.H., Minnet, H.C., 1949. Microwave thermal radiation from the Moon. *Austr. J. Sci. Res.* 2 (1), 63–77.
- Pieters, C.M., et al., 2009. Character and spatial distribution of OH/H₂O on the surface of the Moon seen by M³ on Chandrayaan-1. *Science* 326, 568–572.
- Poston, M.J., Grieves, G.A., Aleksandrov, A.B., Hibbitts, C.A., Dyar, M.D., Orlando, Th.M., 2015. Temperature programmed desorption studies of water interactions with Apollo lunar samples 12001 and 72501. *Icarus* 255, 24–29.
- Prem, P., Artemieva, N.A., Goldstein, D.B., Varghese, P.L., Trafton, L.M., 2015. Transport of water in a transient impact-generated lunar atmosphere. *Icarus* 255, 148–158.
- Ran, Z., Wang, Z., 2014. Simulations of lunar equatorial regolith temperature profile based on measurements of diviner on lunar reconnaissance orbiter. *Sci. China-Earth Sci.* 57 (9), 2232–2241.
- Saal, A.E., et al., 2008. Volatile content of lunar volcanic glasses and the presence of water in the Moon's interior. *Nature* 454 (7201), 192–195.
- Scholten, F., Oberst, J., Matz, K.-D., Roatsch, T., Wählisch, M., Speyerer, E.J., Robinson, M.S., 2012. GLD100: The near-global lunar 100 m raster DTM from LROC WAC stereo image data. *J. Geophys. Res.* 117 (E12). doi:10.1029/2011JE003926.
- Schörghofer, N., 2014. Migration calculations for water in the exosphere of the Moon: dusk-dawn asymmetry, heterogeneous trapping, and D/H fractionation. *Geophys. Res. Lett.* 41, 4888–4893. doi:10.1002/2014GL060820.
- Schörghofer, N., Aharonson, O., 2014. The lunar thermal ice pump. *The Astrophys. J.* 788, 7 article id. 169.
- Shevchenko, V.V., 1996. Swirl patterns on the Moon as traces of a cometary shower. *Solar Syst. Res.* 30 (1), 59–73.
- Shevchenko, V.V., 1999. On the cometary origin of the lunar ice. *Solar Syst. Res.* 33 (5), 456–465.
- Shkuratov, Y., Kaydash, V., Korokhin, V., Velikodsky, Y., Opanasenko, N., Videen, G., 2011. Optical measurements of the Moon as a tool to study its surface. *Planet. Sp. Sci.* 59, 1326–1371. doi:10.1016/j.pss.2011.06.011.
- Simpson, R.A., Tyler, G.L., 1999. Reanalysis of clementine bistatic radar data from the lunar South Pole. *J. Geophys. Res.* 104 (E2), 3845–3862.
- Starukhina, L.V., Shkuratov, Y.G., 2000. The lunar poles: water ice or chemically trapped hydrogen? *Icarus* 147 (2), 585–587 doi:10.1006/icar.2000.6476.
- Starukhina, L.V., 2006. Polar regions of the moon as a potential repository of solar-wind-implanted gases. *Adv. Space Res.* 37, 50–58.
- Starukhina, L., 2012. Water on the Moon: what is derived from the observations?. In: Badescu, V. (Ed.) *Moon: Prospective Energy and Material Resources*. Springer, Heidelberg, Germany, pp. 57–85. Chap. 3.
- Sullivan, M., 2011. version 1.10. Technical Report, diviner.ucla.edu/docs/Diviner_RDR_SIS_1.10.doc. University of California at Los Angeles.
- Sunshine, J.M., Farnham, T.L., Feaga, L.M., Groussin, O., Merlin, F., Milliken, R.E., A'Hearn, M.F., 2009. Temporal and spatial variability of lunar hydration as observed by the deep impact spacecraft. *Science* 326 (5952), 565–568.
- Taylor, L.A., Pieters, C., Morris, R.V., Keller, L.P., McKay, D.S., Patchen, A., Wentworth, S., 1999. Integration of the chemical and mineralogical characteristics of lunar soils with reflectance spectroscopy. *Lunar Planet. Sci. XXX Abstract No.* 1859.
- Ueno, S., Mukai, T., Azuma, H., 1991. Temperature distribution in the permanently shadowed area in lunar polar regions. In: *Proceedings of 24th ISAS Lunar and Planetary Symposium*. Tokyo. ISAS, pp. 190–196.
- Vasavada, A.R., Paige, D.A., Wood, S.E., 1999. Near - surface temperatures on Mercury and the Moon and the stability of polar ice deposits. *Icarus* 141 (2), 179–193. doi:10.1006/icar.1999.6175.
- Vasavada, A.R., Bandfield, J.L., Greenhagen, B.T., Hayne, P.O., Siegler, M.A., Williams, J.-P., Paige, D.A., 2012. Lunar equatorial surface temperatures and regolith properties from the diviner lunar radiometer experiment. *J. Geophys. Res.* 117, 1–12. doi:10.1029/2011JE003987.
- Wang, J., Wu, C., Qiu, Y.L., Meng, X.M., Cai, H.B., Cao, L., Deng, J.S., Han, X.H., Wei, J.Y., 2015. An unprecedented constraint on water content in the sunlit lunar exosphere seen by lunar-based ultraviolet telescope of Chang'e-3 mission. *Planet. Space Sci.* 109, 123–128.
- Watson, K., Murray, B., Brown, H., 1961. On the possible presence of ice on the Moon. *J. Geophys. Res.* 66, 1598–1600.
- Williams, J.-P., Paige, D.A., Greenhagen, B.T., Sefton-Nash, E., 2017. The global surface temperatures of the Moon as measured by the diviner lunar radiometer experiment. *Icarus* 283, 300–325.
- Wöhler, C., Grumpe, A., Berezhnoy, A., Bhatt, M.U., Mall, U., 2014. Integrated topographic, photometric and spectral analysis of the lunar surface: application to impact melt flows and ponds. *Icarus* 235, 86–122.
- Wurz, P., Rohrer, U., Whitby, J.A., Kolb, C., Lammer, H., Dobnikar, P., Martín-Fernández, J.A., 2007. The lunar exosphere. *Sputt. Contrib.* 191, 486–496.
- Zhang, J.A., Paige, D.A., 2009. Cold-trapped organic compounds at the poles of the Moon and Mercury: implications for origins. *Geophys. Res. Lett.* 36 CitelID L16203.
- Zevenbergen, L.W., Thorne, C.R., 1987. Quantitative analysis of land surface topography. *Earth Surf. Process. Landf.* 12 (1), 47–56.